

1 **Targeted degradation of BRD9 reverses oncogenic gene**  
2 **expression in synovial sarcoma**

3

4 Gerard L. Brien<sup>1,11</sup>, David Remillard<sup>2,5</sup>, Junwei Shi<sup>3</sup>, Matthew L. Hemming<sup>1, 2</sup>,  
5 Jonathon Chabon<sup>1</sup>, Kieran Wynne<sup>4</sup>, Eugène T. Dillon<sup>4</sup>, Gerard Cagney<sup>4</sup>, Guido Van  
6 Mierlo<sup>5,6</sup>, Marijke P Baltissen<sup>5</sup>, Michiel Vermeulen<sup>5,6</sup>, Jun Qi<sup>7</sup>, Stefan Fröhling<sup>8,9,10</sup>,  
7 Nathanael S. Gray<sup>7</sup>, James E. Bradner<sup>2,†</sup>, Christopher R. Vakoc<sup>11</sup> and Scott A.  
8 Armstrong<sup>1</sup>

9

10 <sup>1</sup>Department of Pediatric Oncology, Dana Farber Cancer Institute, Boston Children's  
11 Hospital and Harvard Medical School, Boston, MA 02115, USA.

12 <sup>2</sup>Department of Medical Oncology, Dana Farber Cancer Institute, Boston, MA 02215,  
13 USA.

14 <sup>3</sup>Department of Cancer Biology, Abramson Family Cancer Research Institute,  
15 Perelman School of Medicine, University of Pennsylvania, Philadelphia, PA 19104,  
16 USA.

17 <sup>4</sup>School of Biomolecular and Biomedical Science and Conway Institute, University  
18 College Dublin, Belfield, Dublin 4, Ireland.

19 <sup>5</sup>Department of Molecular Biology, Faculty of Science, Radboud Institute for  
20 Molecular Life Sciences, Radboud University Nijmegen, Nijmegen, The Netherlands

21 <sup>6</sup>Department of Molecular Biology, Faculty of Science, Radboud Institute for  
22 Molecular Life Sciences, [OncoCode Institute](#), Radboud University Nijmegen, Nijmegen,  
23 The Netherlands

24 <sup>6</sup>Department of Cancer Biology, Dana Farber Cancer Institute, Boston, MA 02215.

25 <sup>7</sup>Division of Translational Oncology, National Center for Tumor Diseases (NCT)  
26 Heidelberg and German Cancer Research Center (DKFZ), 69120, Heidelberg,  
27 Germany.

28 <sup>8</sup> German Cancer Consortium (DKTK), 69120, Heidelberg, Germany.

29 <sup>9</sup> Section for Personalized Oncology, Heidelberg University Hospital, 69120,  
30 Heidelberg, Germany.

31 <sup>10</sup>Cold Spring Harbor Laboratory, Cold Spring Harbor, NY 11724, USA.

32 <sup>11</sup>Smurfit Institute of Genetics, Trinity College Dublin, Ireland.

33 † Present address: Novartis Institutes for BioMedical Research, Cambridge, MA  
34 02139, USA.

35

36

37 **Correspondence may be addressed to:**

38 Gerard L. Brien PhD - Email: [gbrien@tcd.ie](mailto:gbrien@tcd.ie)

39 Scott A. Armstrong MD, PhD - Email: [scott\\_armstrong@dfci.harvard.edu](mailto:scott_armstrong@dfci.harvard.edu)

40 **Abstract**

41 Synovial sarcoma tumours contain a characteristic fusion protein, SS18-SSX, which  
42 drives disease development. Targeting oncogenic fusion proteins presents an  
43 attractive therapeutic opportunity. However, SS18-SSX has proven intractable for  
44 therapeutic intervention. Using a domain-focused CRISPR screen we identified the  
45 bromodomain of BRD9 as a critical functional dependency in synovial sarcoma.  
46 BRD9 is a component of SS18-SSX containing BAF complexes in synovial sarcoma  
47 cells; and integration of BRD9 into these complexes is critical for cell growth.  
48 Moreover BRD9 and SS18-SSX co-localize extensively on the synovial sarcoma  
49 genome. Remarkably, synovial sarcoma cells are highly sensitive to a novel small  
50 molecule degrader of BRD9, while other sarcoma subtypes are unaffected.  
51 Degradation of BRD9 induces downregulation of oncogenic transcriptional programs  
52 and inhibits tumour progression *in vivo*. We demonstrate that BRD9 supports  
53 oncogenic mechanisms underlying the SS18-SSX fusion in synovial sarcoma and  
54 highlight targeted degradation of BRD9 as a potential therapeutic opportunity in this  
55 disease.

56

57

58

59

60

61

62

63

64

65

66

67

68

69

70

71



72

73

74

75 **Introduction**

76 Sarcomas although rare in adult patients account for up to 20% of all paediatric  
77 malignancies (1). These are often aggressive diseases which do not respond well to  
78 conventional therapeutic interventions (2). As such the cure rates for many of these  
79 diseases are unsatisfactory and patient prognoses remain poor. The molecular  
80 pathology of many of these cancers is associated with recurrent chromosomal  
81 rearrangements; leading to the generation of chimeric fusion proteins. Significantly,  
82 many fusion protein generating aberrations occur in a genomic background with few  
83 co-occurring genetic alterations (3–8). This has led to the prevailing notion that these  
84 gene fusions are often the primary driver of disease development. These  
85 chromosomal rearrangements often effect genes involved in  
86 transcriptional/chromatin regulatory mechanisms; with the resulting fusion proteins  
87 thought to drive disease development by altering the dynamics of transcriptional  
88 control. Excitingly, recent work has highlighted the therapeutic potential of targeting  
89 mechanisms of transcriptional control in cancer cells (9). However, effective means  
90 of blocking oncogenic transcriptional mechanisms in fusion gene driven sarcomas  
91 are currently lacking.

92

93 Synovial sarcoma is a fusion gene driven malignancy, which accounts for ~10% of  
94 soft-tissue sarcomas. Synovial sarcoma is a poorly differentiated malignancy with an  
95 often aggressive clinical progression. It occurs in patients of all ages, but is  
96 particularly common in children and young adults with a peak incidence between 20-  
97 30 years of age. The hallmark genetic abnormality in synovial sarcoma is a recurrent  
98 t(X;18) chromosomal rearrangement. This fuses the *SS18* gene (also known as  
99 *SYT*) on chromosome 18 to one of three related genes *SSX1*, *SSX2* and *SSX4* on  
100 the X chromosome(10–12). This fusion is considered pathognomonic for the  
101 disease, with diagnoses confirmed by RT-PCR and karyotyping analyses to identify  
102 the fusion event. As such, essentially 100% of synovial sarcoma tumours contain an  
103 *SS18-SSX* fusion. The *SS18-SSX* rearrangement is often the only genetic  
104 abnormality in synovial sarcoma tumours (13, 14); suggesting that it is the primary  
105 driver of disease. Indeed, conditional expression of *SS18-SSX* in muscle progenitor

106 cells leads to development of a fully penetrant synovial sarcoma like disease in mice  
107 (15).

108

109 The SS18-SSX fusion protein is believed to function as an aberrant transcriptional  
110 regulator. The SS18 protein is a dedicated component of the chromatin remodelling  
111 BAF (also known as SWI/SNF) complex which functions primarily in transcriptional  
112 activation (16, 17). Whereas the SSX proteins are thought to function in gene  
113 silencing; potentially through interactions with the Polycomb Repressive Complex  
114 (PRC)1 (18, 19). SS18-SSX dominantly assembles into BAF complexes in synovial  
115 sarcoma cells, leading to eviction of the wildtype SS18 and SNF5 proteins from the  
116 complex. This altered complex assembly is redistributed on chromatin and drives an  
117 expression signature required to maintain the proliferative/undifferentiated state of  
118 synovial sarcoma cells (20, 21). SS18-SSX chromatin binding is directed in part  
119 through interactions with the PRC1.1 complex; mediated by the SSX portion of the  
120 fusion (21). The recruitment of SS18-SSX to chromatin via interactions with PRC1.1  
121 is essential for the oncogenic function of the fusion. Moreover, association of SS18-  
122 SSX with DNA-binding transcription factors has also been suggested to be important  
123 for chromatin binding and oncogenic activities (22). Recruitment of BAF complex  
124 activity to SS18-SSX bound regions is essential for transcriptional activation of fusion  
125 target genes (20, 21, 23). Depletion of SS18-SSX protein levels leads to reduced  
126 BAF complex binding at target sites and repression of fusion target genes. These  
127 findings highlight that SS18-SSX driven alterations in chromatin regulatory pathways  
128 are a key aspect of synovial sarcoma oncogenesis. Moreover, they highlight that  
129 targeting mechanisms related to fusion protein recruitment and BAF complex  
130 function may provide a therapeutic opportunity in this disease. However, to date  
131 robust approaches for targeting these mechanisms have not been described.

132

133 Here using a custom CRISPR/Cas9 based functional genomics approach focused on  
134 chromatin regulatory genes we identify the bromodomain of BRD9 as a vulnerability  
135 in synovial sarcoma cells. We show that BRD9 is part of SS18-SSX containing BAF  
136 complexes in synovial sarcoma cells; and that the association of BRD9 with the BAF  
137 complex is functionally essential. Targeting BRD9 with a novel chemical degrader  
138 specifically impedes synovial sarcoma cell viability; eliciting more robust therapeutic  
139 effects than BRD9 inhibition using bromodomain targeting chemical probes.

140 Importantly, BRD9 is required to maintain appropriate expression of an oncogenic  
141 gene expression signature driven by SS18-SSX. Taken together, our findings  
142 highlight BRD9 as a novel therapeutic target in synovial sarcoma.

143

144

## 145 **Results**

### 146 **The BRD9 bromodomain is a functional dependency in synovial sarcoma**

147 To identify functional chromatin based dependencies that may be amenable to  
148 therapeutic targeting in synovial sarcoma cells we used a CRISPR/Cas9 based  
149 domain focused pooled screening approach (24). To this end we generated a  
150 custom lentiviral sgRNA library targeting known functional regions in 193 chromatin  
151 regulatory proteins. Viral supernatants generated with this library were used to infect  
152 Cas9 expressing synovial and Ewing sarcoma cell lines. The relative abundance of  
153 individual sgRNAs within each population was compared between early and late time  
154 points by high-throughput sequencing (Figure 1A). These analyses demonstrated  
155 that 3 independent sgRNAs targeting the bromodomain of BRD9 were depleted from  
156 synovial, but not Ewing sarcoma cell cultures (Figure 1B-C, and Figure 1-source  
157 data 1 and 2). Remarkably, of the 52 bromodomains contained within 38 proteins  
158 targeted in this library, only the BRD9 bromodomain had all sgRNAs specifically  
159 depleted in synovial sarcoma cells (Figure 1-figure supplement 1A). This is in striking  
160 contrast to the bromodomains of BRD4 which are a dependency in both synovial and  
161 Ewing sarcoma cells, as well as several other malignancies (25, 26). To further  
162 examine the specificity of this dependency we performed individual sgRNA depletion  
163 assays in 2 independent synovial, Ewing and rhabdomyosarcoma cell lines,  
164 respectively. These experiments demonstrated that BRD9 bromodomain targeting  
165 sgRNAs were only depleted in synovial sarcoma cells (Figure 1D and Figure 1-  
166 source data 3). Importantly, the sgRNAs used here have comparable or higher  
167 genome editing efficiencies in Ewing and rhabdomyosarcoma cell lines, compared to  
168 synovial sarcoma cells (Figure 1-figure supplement 1B and data not shown). This  
169 indicates that differences in sgRNA depletion cannot be attributed to discrepancies in  
170 sgRNA editing. Moreover, BRD9 expression levels are consistent across all cell lines  
171 tested, indicating that differences in BRD9 levels do not reflect altered sensitivity to  
172 BRD9 targeting (Figure 1-figure supplement 1C). Using an independent shRNA-  
173 based approach we observed similar synovial sarcoma specific effects following

174 knockdown of BRD9 protein levels (Figure 1-figure supplement 1D-G). Consistent  
175 with this, within the recently published Project DRIVE (27) database we observe, that  
176 among the almost 400 cancer cell lines assayed, synovial sarcoma cell lines are the  
177 most sensitive to BRD9 targeting (Figure 1E). To confirm the importance of the  
178 BRD9 bromodomain we performed functional rescue experiments. We generated a  
179 full-length human BRD9 cDNA containing silent point mutations within the sgRNA  
180 recognition sequence, conferring resistance to Cas9 targeting (Figure 1-figure  
181 supplement 1H). Next, we expressed a full-length (FL), bromodomain deleted  
182 ( $\Delta$ bromo) or bromodomain inactivated (N216A) version of this cDNA in synovial  
183 sarcoma cells. This demonstrated that only wildtype full-length BRD9 can rescue the  
184 depletion of sgRNAs targeting the bromodomain (Figure 1F, Figure 1-source data 4,  
185 Figure 1-figure supplement 1I). This indicates that BRD9, and the BRD9  
186 bromodomain, are selective functional dependencies in synovial sarcoma;  
187 highlighting a novel therapeutic target in this disease.

188

### 189 **BRD9 is a component of SS18-SSX containing BAF complexes**

190 BRD9 has previously been shown to be a component of the BAF complex in several  
191 normal tissues (28). Moreover, biochemical studies in HEK293T cells have indicated  
192 that BRD9 can also associate with SS18-SSX containing complexes in this setting  
193 (16). However, it is unknown whether BRD9 is part of the oncogenic SS18-SSX  
194 containing BAF complex in synovial sarcoma cells. Consistent with previous results  
195 we found that BRD9 associates with exogenously expressed SS18-SSX1/2 in  
196 HEK293T cells (Figure 2-figure supplement 1A-C, Figure 2-figure supplement-source  
197 data 1-3). Next, to test whether SS18-SSX fusions also interact with BRD9 in  
198 synovial sarcoma cells, we immunoprecipitated the endogenous fusion protein in 2  
199 independent synovial sarcoma cell lines (Figure 2A). Significantly, these experiments  
200 demonstrated that BRD9 co-purifies with endogenous SS18-SSX containing BAF  
201 complexes in synovial sarcoma cells (Figure 2B, Figure 2-source data 1 and 2,  
202 Figure 2-figure supplement 1D and Figure 2-figure supplement 1-source data 4).  
203 Moreover, SS18-SSX fusion proteins co-purify with BRD9 in reciprocal endogenous  
204 IP experiments (Figure 2C and D). A recent report indicates that BRD9 is a member  
205 of a novel subclass of BAF complex(es), termed GBAF (for GLTSCR1/1L-BAF) (29).  
206 These complexes lack SNF5 and an ARID component and contain BRD9, GLTSCR1

207 or GLTSCR1L as defining complex members. Our proteomic analysis of endogenous  
208 SS18-SSX containing complexes identified peptides mapping to GLTSCR1, lending  
209 support to the notion that the fusion incorporates into GBAF assemblies containing  
210 BRD9 (Figure 2-figure supplement 1C and D). As such by combining genomic and  
211 proteomic approaches we have identified BRD9 as a functional dependency within  
212 SS18-SSX fusion protein containing BAF complexes in synovial sarcoma cells.

213

214 To ascertain the relative proportion of individual BAF complex members in SS18-  
215 SSX purifications we used the intensity-based absolute quantification (iBAQ)  
216 algorithm (30). This showed that core complex members such as SMARCC1,  
217 SMARCC2 and SMARCA4 have relative abundances approximately equal to, or  
218 greater than, SS18-SSX (Figure 2E); suggesting that these proteins co-exist with the  
219 fusion protein in most (if not all) complexes. However, the relative abundance of  
220 BRD9 (and GLTSCR1) is 10-20% that of SS18-SSX; indicating that these  
221 components are sub-stoichiometric members of SS18-SSX containing complexes.  
222 Interestingly, several of the BAF complex members (PBRM, SMARCA2 and  
223 SMARCA4) identified in these proteomics studies were included in our functional  
224 genomics screen (Figure 1A). However, no robust dependencies were evident  
225 among the bromodomains of these proteins which were targeted within our library  
226 (Figure 2-figure supplement 1E). Intriguingly, this suggests that the minor subset of  
227 BRD9 containing complexes are particularly important, and perhaps functionally  
228 specialised in synovial sarcoma cells.

229

### 230 **BRD9 functions within SS18-SSX containing complexes**

231 Next, we wanted to understand whether BRD9 executes any bromodomain  
232 independent functions in synovial sarcoma cells. To do this we used a high-density  
233 CRISPR mutagenesis approach, introducing 92 individual sgRNAs targeting across  
234 the BRD9 locus into Cas9 expressing synovial sarcoma cell lines. We monitored for  
235 changes in sgRNA expressing (GFP-positive) cells over time, and consistent with our  
236 pooled screen most sgRNAs targeting the BRD9 bromodomain were robustly out  
237 competed in these GFP depletion assays (Figure 2F and Figure 2-source data 3).  
238 However, we identified an additional hotspot of sgRNA depletion within a previously  
239 uncharacterised central region of BRD9 (amino acids 311-345). We confirmed the  
240 importance of this region with functional rescue experiments showing that a  $\Delta$ 311-

241 345 BRD9 cDNA was incapable of rescuing the depletion of sgRNAs targeting this  
242 region (Figure 2G and Figure 2-source data 4). Strikingly, co-IP experiments found  
243 that while the BRD9 bromodomain is dispensable for BAF complex interaction, this  
244 novel functional region is essential for association with the complex (Figure 2H).  
245 These results identify a novel BAF complex interaction domain within BRD9 and  
246 demonstrate that association of BRD9 with the BAF complex is functionally essential  
247 in synovial sarcoma cells.

248

### 249 **BRD9 co-binds the synovial sarcoma genome with SS18-SSX**

250 To understand the extent to which BRD9 and SS18-SSX containing complexes  
251 overlap on chromatin we performed chromatin immunoprecipitation with next-  
252 generation sequencing (ChIP-seq). Owing to a lack of high-quality ChIP-grade  
253 antibodies for BRD9 and SS18-SSX, we adapted a previously reported  
254 CRISPR/Cas9 based approach to knock-in a 3xHA epitope tag at the C-termini of  
255 the endogenous *BRD9* and *SS18-SSX1* loci in HSSYII cells (31) (Figure 3-figure  
256 supplement 1A). ChIP-seq analyses demonstrated that BRD9 and SS18-SSX1 bind  
257 broadly throughout the genome (Figure 3A); with ~35% of binding sites occurring at  
258 gene promoters and the remaining ~65% at distal inter- and intragenic regions  
259 (Figure 3B). Comparing the binding profiles of BRD9 and SS18-SSX1 demonstrated  
260 that these proteins co-localize extensively on the synovial sarcoma genome. Indeed,  
261 a clear majority of all identified BRD9 and SS18-SSX1 binding sites overlap (Figure  
262 3C), and there is a tight correlation in BRD9 and SS18-SSX1 occupancy genome-  
263 wide (Figure 3-figure supplement 1B). Additional ChIP-seq analyses of RNA  
264 polymerase II (RNAPII) and the histone modification H3K27Ac further demonstrates  
265 that BRD9 and SS18-SSX1 bind virtually all active gene promoters and enhancer  
266 elements (Figure 3D and E). With little evidence of significant binding at inactive  
267 genomic loci. Two recent studies characterised gene expression signatures defining  
268 synovial sarcoma tumours, demonstrating that the SS18-SSX fusion directly binds  
269 many of these genes (20, 21). Importantly, we found a significant overlap between  
270 these previous SS18-SSX1 ChIP studies and our own epitope tag knock-in mediated  
271 SS18-SSX1 and BRD9 ChIP-seq experiments (Figure 3F and Figure 3-figure  
272 supplement 1C). Considering that BRD9 may be present in only ~15% of SS18-SSX  
273 containing complexes, such broad co-localisation is remarkable; and suggests BRD9

274 containing complexes play an important role in supporting SS18-SSX function  
275 genome-wide.

276

### 277 **BRD9 bromodomain inhibition**

278 Several recent studies have described the development of potent small-molecule  
279 inhibitors of the BRD9 bromodomain (32–34). To test the feasibility of small-molecule  
280 mediated targeting of the BRD9 bromodomain as a therapeutic approach in synovial  
281 sarcoma we performed dose response experiments using two independent BRD9  
282 inhibitors, BI7273 and I-BRD9. Consistent with our genetic data, synovial sarcoma  
283 cells were more sensitive to BRD9 bromodomain inhibition compared to other  
284 pediatric sarcomas (Figure 4A). However, these effects were modest with growth  
285 IC50 values in the  $\mu\text{M}$  range. Interestingly, spike-in normalized BRD9 ChIP-seq  
286 (ChIP-Rx) performed in BI7273 treated cells demonstrated that while the chromatin  
287 occupancy of BRD9 is reduced in inhibitor treated cells some BRD9 remains  
288 associated with chromatin (Figure 4B). This indicates that BRD9 does not rely  
289 exclusively on bromodomain function to associate with chromatin. Consistent with  
290 this, mutational inactivation of the BRD9 bromodomain also leads to an incomplete  
291 loss of BRD9 binding across the genome (Figure 4-figure supplement 1A and B).  
292 Significantly, the ability of BRD9 to incorporate into the BAF complex is required for  
293 chromatin association, since deleting the BAF complex interaction domain (aa311-  
294 345) leads to a similar reduction in chromatin binding as bromodomain deletion  
295 (Figure 4C and Figure 4-source data 1). Taken together, these data indicate that  
296 BRD9, as part of the BAF complex, can access chromatin in a bromodomain  
297 independent manner. Highlighting that bromodomain inhibition, while at least partially  
298 effective at blocking synovial sarcoma cell growth/survival, is unlikely to completely  
299 ablate the functional contributions of BRD9.

300

### 301 **Targeted degradation of the BRD9 protein**

302 To completely inactivate BRD9 function we leveraged our recent success developing  
303 a targeted chemical degrader of BRD9 (35). We created an optimized chemical  
304 analogue of our previous BRD9 degrader, dBRD9-A (Figure 4D). This molecule  
305 contains a more lipophilic alkyl linker and exhibits improved BRD9 degradation  
306 properties (data not shown). Importantly, dBRD9-A is a highly specific binder of the

307 BRD9 bromodomain (Figure 4E); and elicits near complete BRD9 degradation at low  
308 nanomolar concentrations (Figure 4F). These degradation effects are dependent on  
309 the E3 ubiquitin ligase component CRBN, as well as BRD9 bromodomain  
310 engagement (Figure 4-figure supplement 1B-C). ChIP-Rx experiments demonstrate  
311 a far more robust loss of BRD9 binding across the genome following dBRD9-A  
312 treatment; compared to BI7273 treatment (Figure 4G). Indeed, essentially no BRD9  
313 remains bound on chromatin following 24hrs of dBRD9-A treatment (Figure 4H).  
314 Significantly, BRD9 degradation leads to a greater therapeutic response than  
315 bromodomain inhibition (Figure 4I); consistent with the notion that BRD9 also  
316 functions independently of its bromodomain. Moreover, consistent with our genetic  
317 data other pediatric sarcoma subtypes are unaffected by BRD9 degradation (Figure  
318 4-figure supplement 1E-F). Interestingly, the observed increase in therapeutic  
319 response in dBRD9-A treated cells is not due to destabilisation of the SS18-SSX  
320 fusion itself (Figure 4-figure supplement 1G). However, quantitative interactions  
321 proteomics of SS18-SSX containing complexes in dBRD9-A treated cells  
322 demonstrate that the GBAF members (GLTSCR1/L), in addition to BRD9, are lost  
323 from fusion protein containing complexes following BRD9 degradation (Figure 4-  
324 figure supplement 1H). This suggests that BRD9 is essential for the proper assembly  
325 of GBAF complexes; and that BRD9 degradation specifically disrupts this subclass of  
326 SS18-SSX containing complexes. Taken together, these data demonstrate that  
327 targeting BRD9 function with chemical degraders, rather than bromodomain  
328 inhibitors, is a more efficacious therapeutic approach in synovial sarcoma.

329

### 330 **BRD9 supports oncogenic transcription in synovial sarcoma**

331 Synovial sarcoma cells treated with dBRD9-A undergo a progressive cell cycle arrest  
332 (Figure 5A and Figure 5-source data 1), which is further associated with an increase  
333 in Annexin-V positivity (Figure 5B and Figure 5-source data 3). Consistent with the  
334 on-target activity of dBRD9-A, swapping the BRD9 bromodomain for the closely  
335 related BRD7 bromodomain (63%, sequence identity) renders BRD9 and synovial  
336 sarcoma cells insensitive to dBRD9-A treatment (Figure 5-figure supplement 1A-B  
337 and Figure 5-figure supplement 1-source data 1). Using an *in vivo* synovial sarcoma  
338 xenograft model, we found that treatment of mice with dBRD9-A over 24 days  
339 inhibited tumour progression (Figure 5C). We confirmed *in vivo* pharmacodynamic  
340 activity of dBRD9-A in this system by immunoblotting BRD9 in tumour tissue derived



341 from vehicle and dBRD9-A treated mice (Figure 5D). Mice treated with dBRD9-A did  
342 not suffer any overt side effects associated with treatment, retaining a normal body  
343 weight and blood counts (Figure 5-figure supplement 1C-D and and Figure 5-figure  
344 supplement 1-source data 2-3). Next we performed cell count normalized RNA-seq  
345 analysis to understand why synovial cells are effected by BRD9 degradation. We  
346 performed these experiments 6hrs after dBRD9-A treatment (the earliest time point  
347 where we observe complete BRD9 degradation) to allow characterisation of the  
348 primary molecular changes following BRD9 loss. Strikingly, degradation of BRD9  
349 primarily leads to down regulated gene expression (Figure 5E and Figure 5-source  
350 data 3). Using our H3K27Ac ChIP-seq data we identified the subset of genes  
351 associated with super enhancer (SE) elements; since studies have demonstrated  
352 that SE-associated genes are highly sensitive to transcriptional perturbation.  
353 Moreover, SEs drive expression of genes required for maintaining tumour cell  
354 identity (36, 37). Consistent with this, several genes associated with SEs in HSSYII  
355 cells including TWIST1 (38) and TLE1 (22) are known to play key functional roles in  
356 synovial sarcoma (Figure 5F). Moreover, expression of many of these genes has  
357 previously been linked to primary synovial sarcoma tumour phenotypes, defining  
358 both clinical and biological characteristics (20, 21, 39–43). SEs have higher BRD9  
359 and SS18-SSX1 occupancy levels compared to typical enhancers (Figure 5-figure  
360 supplement 1E); and BRD9 degradation leads to a preferential downregulation of SE  
361 associated gene expression (Figure 5G). Significantly, these genes depend on  
362 SS18-SSX1 to maintain their expression, since shRNA mediated knockdown of  
363 SS18-SSX1 leads to a collapse of SE associated gene expression (Figure 5H).  
364 dBRD9-A treatment and consequential downregulation of transcription is further  
365 associated with reductions in SS18-SSX1 binding at SEs (Figure 5I and Figure 5-  
366 figure supplement 1F). Interestingly, since SS18-SSX1 and BRD9 directly bind the  
367 majority of active genes, these transcriptional perturbations amount to a relatively  
368 narrow impingement on the broader cohort of SS18-SSX downstream target genes  
369 (Figure 5-figure supplement 1G). However, these data demonstrate that BRD9 is  
370 required to maintain the SE associated oncogenic transcriptional program driven by  
371 SS18-SSX and the phenotypic impact of BRD9 degradation underlines the functional  
372 importance of this gene cohort. Most importantly, these data show that targeting  
373 BRD9 using our novel degrader compound directly perturbs underlying oncogenic  
374 mechanisms in this disease.

375

376 **Discussion**

377 We've shown that BRD9 is an essential SS18-SSX fusion protein co-factor in  
378 synovial sarcoma. Our data indicate that through assembly into SS18-SSX  
379 containing complexes BRD9 supports oncogenic gene expression programs  
380 necessary for synovial sarcoma oncogenesis. This is likely achieved, at least in part,  
381 via bromodomain mediated interactions with chromatin regions marked with acetyl-  
382 lysine modifications. Indeed, we observe the greatest amount of BRD9 and SS18-  
383 SSX binding at super enhancer elements associated with high levels of H3K27Ac.  
384 BRD9 may promote and/or stabilize binding of SS18-SSX containing complexes at  
385 acetylated chromatin regions; since loss of BRD9 can lead to reduced fusion protein  
386 occupancy at some super enhancers. This induces perturbations of oncogenic gene  
387 expression programs driven by the fusion protein and robust therapeutic effects. This  
388 work highlights the first actionable therapeutic vulnerability, directly linked to SS18-  
389 SSX, in synovial sarcoma. These findings provide a rationale for future clinical  
390 investigations of BRD9 as a therapeutic target in synovial sarcoma patients.

391

392 This work demonstrates that direct targeting of oncogenic, SS18-SSX containing  
393 BAF complexes is a viable therapeutic approach in synovial sarcoma. Recent work  
394 has indicated that BRD9 assembles into a previously unreported form of the BAF  
395 complex, termed GBAF (29). This complex is defined by the presence of either  
396 GLTSCR1 or GLTSCR1L and BRD9; and also lacks SNF5 and an ARID component.  
397 This altered complex assembly suggests potential functional specialization within  
398 BRD9 containing complexes. Therefore, it will be important to perform detailed  
399 structure/function studies to better understand the molecular contributions of these  
400 novel complexes. Interestingly, our finding that GLTSCR1 and GLTSCR1L are lost  
401 from SS18-SSX containing complexes following BRD9 degradation already suggests  
402 that BRD9 is essential for assembly of GBAF complexes. The specificity of the  
403 observed dependency on BRD9 containing complexes in synovial sarcoma cells is  
404 quite remarkable and bodes well for potential clinical applications in patients.  
405 Interestingly, a recent report indicated that malignant rhabdoid tumour (MRT) cells  
406 are also dependent on BRD9 function (44). Interestingly, MRTs and synovial  
407 sarcoma share a common feature, that being loss of SNF5. In essentially 100% of  
408 MRTs *SNF5* is subject to biallelic inactivation; while in synovial sarcoma assembly of

409 SS18-SSX into BAF complexes leads to eviction and proteasomal degradation of  
410 SNF5. Since SNF5 is absent in BRD9 containing complexes it is tempting to  
411 speculate that loss of SNF5 (by genetic or biochemical means) shifts the balance of  
412 BAF complex assembly to a more GBAF-like state. This could explain the shared  
413 dependency on BRD9 function in these malignancies. Several additional cancers,  
414 including bladder cancer and uterine corpus endometrial carcinoma, have a high  
415 frequency of mutations effecting the genes encoding ARID1A/B (45). Loss of  
416 function mutations in these components could potentially shift the dynamics of BAF  
417 complex assembly toward a GBAF-like state. Therefore, it will be important to test  
418 the efficacy of BRD9 targeting in other cancers with BAF complex mutations.

419

420 Most cancer treatments target processes important in normal and cancer cells,  
421 therefore toxicities resulting in debilitating side-effects remains problematic. Fusion  
422 gene driven cancers present a relatively unique opportunity to target cancer cell  
423 specific processes since oncogenic fusion proteins are present only in malignant  
424 cells. Understanding mechanisms related to fusion protein function may provide  
425 opportunities to develop therapies targeting underlying pathologies with limited  
426 effects on normal tissues. Our work demonstrates the importance of BRD9 in  
427 supporting SS18-SSX function and oncogenic gene expression in synovial sarcoma  
428 cells. Currently synovial sarcoma has few effective treatment options, and advanced  
429 forms of the disease have very poor overall survival. This study provides a rationale  
430 for development of BRD9 degradation as a novel therapeutic approach and  
431 potentially assessment in patients suffering with this disease. We demonstrate that  
432 degradation of BRD9, a member of an oncogenic multi-protein complex in synovial  
433 sarcoma, has a more profound effect on cancer cell survival than small-molecule  
434 mediated inhibition. This is an important point since inhibition of chromatin regulators  
435 such as EZH2, DOT1L and LSD1, which also exist in stable multi-protein complexes  
436 is currently under clinical investigation in several cancers (9, 46). Our findings  
437 suggest that inhibition, while effectively blocking a single functionality within a target  
438 protein, may provide a relatively ineffective means to block protein complex function  
439 as a whole. Scaffolding/other non-inhibited functions of a target protein may remain  
440 unaffected, allowing the target to continue supporting complex function. Therefore,  
441 degradation of proteins within multi-protein complexes may be a more efficacious  
442 approach in many cases. Importantly, the potent and selective small-molecule

443 inhibitors that already exist for proteins such as EZH2 and DOT1L will provide a  
 444 basis for the development of novel protein degraders targeting these proteins.

445

446

447

448

449

## 450 **Materials and Methods**

451

### 452 **Key Resources table:**

Reagent type (species) or resource	Designation	Source or reference	Identifiers	Additional information
cell line ( <i>Homo sapiens</i> )	HEK293T	ATCC	RRID:CVCL_0063	
cell line ( <i>Homo sapiens</i> )	HSSYII			Provided from the laboratory of Stefan Frohling
cell line ( <i>Homo sapiens</i> )	SYO1			Provided from the laboratory of Stefan Frohling
cell line ( <i>Homo sapiens</i> )	1273/99			Provided from the laboratory of Stefan Frohling
cell line ( <i>Homo sapiens</i> )	A673	ATCC	RRID:CVCL_0080	
cell line ( <i>Homo sapiens</i> )	CME1			Provided from the laboratory of Stefan Frohling
cell line ( <i>Homo sapiens</i> )	SKNMC	ATCC	RRID:CVCL_0530	
cell line ( <i>Homo sapiens</i> )	RH30	ATCC	RRID:CVCL_0041	
cell line ( <i>Homo sapiens</i> )	RH41	DSMZ	RRID:CVCL_2176	
antibody	BRD9, rabbit polyclonal	Bethyl Laboratories	RRID:AB_11218396	Western blotting (1:2500) and IP (5µgs)
antibody	HA, rabbit monoclonal	Cell Signalling Technologies	RRIDA:AB_1549585	Western blotting (1:1000) and ChIP (5-10µgs)
antibody	ACTIN, mouse monoclonal	Cell Signalling Technologies	RRID:AB_2750839	Western blotting (1:5000)
antibody	CRBN, rabbit polyclonal	Proteintech	RRID:AB_2085739	Western blotting (1:1000)
antibody	V5, rabbit polyclonal	Bethyl Laboratories	RRID:AB_67586	Western blotting (1:1000)
antibody	SSX1, rabbit polyclonal	MyBioscience	RRID:AB_2750841	IP (10µgs)
antibody	SSX2, rabbit polyclonal	MyBioscience	RRID:AB_2750840	IP (10µgs)
antibody	SS18, rabbit polyclonal	Santa Cruz Biotechnology	RRID:AB_2195154	Western blotting (1:500)
antibody	H3K27Ac, rabbit polyclonal	Abcam	RRID:AB_2118291	ChIP (5µgs)
antibody	RNAPII, mouse	Diagenode	RRID:AB_2750842	ChIP (10µs)

	monoclonal			
other	HA	Pierce	RRID:AB_2749815	IP affinity resin
other	V5	Sigma Aldrich	RRID:AB_10062721	IP affinity resin
chemical compound, drug	dBRD9-A	This study		
chemical compound, drug	BI7273	Cayman Chemical	20311	
chemical compound, drug	I-BRD9	Cayman Chemical	17749	
chemical compound, drug	X-termeGENE 9	Sigma Aldrich	6365809001	
chemical compound, drug	Formaldehyde	Fisher Scientific	BP531-500	
chemical compound, drug	DSG	Pierce	20593	
chemical compound, drug	ATPLite 1-Step	Perkin Elmer	6016731	
recombinant DNA reagent	pPAX2	Addgene	12260	
recombinant DNA reagent	pCMV-VSV-G	Addgene	8454	
recombinant DNA reagent	pLEX305	Addgene	41390	
recombinant DNA reagent	pLEX305-3xHA	This study		
recombinant DNA reagent	LRG2.0T	This study		Provided from the laboratory of Chris Vakoc
recombinant DNA reagent	SGEN	MSKCC RNAi core facility		
recombinant DNA reagent	pCR8	Invitrogen	K250020	
recombinant DNA reagent	pCR8-BRD9 (and derivatives)	This study		
commercial assay or kit	4-12% Bis-Tris gels	Invitrogen	NW04127BOX	
commercial assay or kit	Q5 Site-Directed mutagenesis kit	NEB	E0554S	
commercial assay or kit	ThruPlex DNA-seq kit	Rubicon Genomics	R400427	
commercial assay or kit	Tapestation D1000 screentape	Agilent	5067- 5584	
commercial assay or kit	NextSeq 500 High Output v2	Illumina	FC-404-2005	
commercial assay or kit	RNeasy mini-kit	Qiagen	74106	
commercial assay or kit	ERCC spike-in controls	Ambion	4456740	
commercial assay or kit	NEBNext Ultra RNA library prep kit	NEB	E7530L	
commercial assay or kit	BD Pharmingen BrdU Flow kit	BD	559619	
commercial assay or kit	BD Annexin V Apoptosis detection kit	BD	556547	
software, algorithm	ChIP and RNA-seq analysis	Basepair		<a href="http://www.basepair.io">www.basepair.io</a>
software, algorithm	ChIP-seq data visualisation	EaSeq		<a href="https://easeq.net">https://easeq.net</a>

strain, strain background ( <i>Mus musculus</i> )	BALB/c (Foxn1nu)	Charles River Laboratory	CAnN.Cg-Foxn1nu/Crl	
---	------------------	--------------------------	---------------------	--

453

454

455

456

457

458

459 **Cell culture and lentiviral production:** All cell lines were maintained at 37°C in a  
460 humidified incubator. Lentiviral packaging HEK293T, synovial sarcoma (HSSYII,  
461 SYO1 and 1273/99) and Ewing’s sarcoma (A673) cell lines were cultured in DMEM  
462 (Gibco) media supplemented with 10% heat-inactivated fetal bovine serum (FBS),  
463 1% Penicillin-Streptomycin and 12.5ug/ml Plasmocin. Synovial sarcoma (CME1),  
464 Ewing’s sarcoma (SKNMC) and rhabdomyosarcoma (RH30 and RH41) cells were  
465 cultured in RPMI (Gibco) media supplemented with 10% heat-inactivated fetal bovine  
466 serum (FBS), 1% Penicillin-Streptomycin and 12.5ug/ml Plasmocin. Cell lines were  
467 tested regularly for mycoplasma contamination and tested negative in all cases.  
468 Lentiviral supernatants were generated by co-transfection of HEK293T cells with a  
469 lentiviral expression vector (cDNA, sgRNA or shRNA) with viral packaging (PAX2)  
470 and envelope (VSV-G) vectors using the X-tremegene transfection reagent (Roche)  
471 in accordance with the manufacturer’s instructions. Viral supernatants were collected  
472 between 24-48hrs post-transfection and used directly for infection of target cells after  
473 filtering through a 0.45µm syringe filter and addition of 8.5µg/ml Polybrene.

474

475 **Pooled CRISPR screening and data analysis:** The human epigenetic domain U6-  
476 sgRNA-EFS-GFP targeting library was pooled at equimolar ratio and used to  
477 generate lentiviral supernatant as described above. A dilution series of this virus  
478 correlated with GFP positivity in infected cells, and was used to derive an accurate  
479 viral multiplicity of infection (MOI). The total number of synovial and Ewing’s sarcoma  
480 target cells for infection was chosen to achieve at least 500-fold representation of  
481 each sgRNA in the initially infected cell population. To ensure that a single sgRNA  
482 was transduced per cell, the viral volume for infection was chosen to achieve an MOI  
483 of 0.3–0.4. Genomic DNA was extracted at the indicated time points using QiAamp  
484 DNA mini kit (Qiagen #51304), following the manufacturer’s instructions. To maintain

485 >500× sgRNA library representation, 16–20 independent PCR reactions were used  
486 to amplify the sgRNA cassette, which were amplified for 20 cycles with 100-200ng of  
487 starting gDNA using the 2× Phusion Master Mix (Thermo Scientific #F-548). The  
488 PCR products were pooled and end repaired with T4 DNA polymerase (NEB), DNA  
489 polymerase I (NEB), and T4 polynucleotide kinase (NEB). An A overhang was added  
490 to the end-repaired DNA using Klenow DNA Pol Exo- (NEB). The DNA fragment was  
491 then ligated with diversity-increased barcoded Illumina adaptors followed by 5 pre-  
492 capture PCR cycles. Barcoded libraries were pooled at equal molar ratio and  
493 subjected to massively parallel sequencing using a Mi-Seq instrument (Illumina)  
494 using paired-end 150bp reads (MiSeq Reagent Kit v2; Illumina MS-102-2002). The  
495 sequence data were trimmed to contain only the sgRNA sequence then mapped to  
496 the reference sgRNA library without allowing any mismatches. The read counts were  
497 then calculated for each individual sgRNA. To compare the differential  
498 representation of individual sgRNAs between day 3 and day 15 time points, the read  
499 counts for each sgRNA were normalized to the counts of the negative control  
500 ROSA26 sgRNA.

501

502 **Cloning and mutagenesis:** The human full-length BRD9 cDNA was PCR amplified  
503 from MGC clone 5428011 and inserted in the Gateway cloning compatible entry  
504 vector pCR8/GW/TOPO (Invitrogen, K250020) in accordance with the  
505 manufacturer's instructions. Clone integrity was confirmed by sanger sequence.  
506 Mutagenesis of the wildtype BRD9 sequence was performed using pCR8-BRD9 as  
507 template and the Q5 Site-Directed Mutagenesis Kit (NEB, E0554S) in accordance  
508 with the manufacturer's instructions. Sequence verified BRD9 ORF sequences were  
509 subsequently cloned into the Gateway expression vector pLEX305 (Addgene vector,  
510 41390) which had been engineered to contain an N-terminal 3xHA epitope tag using  
511 LR clonase (Invitrogen, 12538120).

512

513 **Immunoprecipitation:** Immunoprecipitations were performed as previously  
514 described (47). Briefly, nuclear pellets were lysed in buffer C containing protease  
515 inhibitors (20 mM HEPES at pH 7.6, 20% [v/v] glycerol, 0.42 M NaCl, 1.5 mM MgCl<sub>2</sub>,  
516 0.2 mM EDTA, aprotinin 1 μg mL<sup>-1</sup>, leupeptin 10 μg mL<sup>-1</sup>, PMSF 1 mM) and  
517 subsequently dialyzed against buffer C-100 (20 mM HEPES at pH 7.6, 20% [v/v]  
518 glycerol, 0.2 mM EDTA, 100 mM KCl, 1.5 mM MgCl<sub>2</sub>, 0.2 mM EDTA). Antibody-

519 coupled beads were incubated with dialyzed nuclear extracts containing 250 U of  
520 benzonase (Sigma) for 3h at 4°C. Beads were then washed, and elutions were  
521 performed with 1xLDS buffer, 1 mg/mL HA peptide or 1mg/mL V5 peptide (Sigma).

522

523 **Mass spectrometry:** In-solution tryptic digestions were performed as described  
524 previously(48). Peptides were analysed with a Q-Exactive mass spectrometer  
525 coupled with an EASY-nLC HPLC system (Thermo Fisher) and an in-house packed  
526 C18 column (New Objective). Parent ion spectra (MS1) were measured at resolution  
527 70,000, AGC target 3e6. Tandem mass spectra (MS2, up to 10 scans per duty cycle)  
528 were obtained at resolution 17,500, AGC target 5e4, collision energy of 25. All mass  
529 spectrometry data were processed using the MaxQuant software, version 1.3.0.5  
530 (49). The following search parameters were used; Fixed Mod: carbamidomethylation,  
531 Variable Mods: methionine oxidation, Trypsin/P digest enzyme, Precursor mass  
532 tolerances 6 ppm, Fragment ion mass tolerances 20 ppm, Peptide FDR 1%, Protein  
533 FDR 1%.

534

535 **Quantitative interaction proteomics in dBRD9-A treated cells:**

536 **On bead digestion and mass spectrometry**

537 After the pulldown, the beads were resuspended in elution buffer (2M Urea, 100 mM  
538 Tris pH 8, 10 mM DTT) and incubated 20 min on a shaker (1300 rpm) at RT. After  
539 incubation, iodoacetamide was added to a final concentration of 50 mM, followed by  
540 10 min shaking in the dark at RT. Partial digestion and elution from the beads was  
541 initiated by adding 0.25 µg Trypsin (Promega; V5113) for 2 hours. The supernatant  
542 containing the IP samples was collected and the beads were resuspended in 50 µl  
543 elution buffer followed by a 5 min incubation shaking at RT. Both supernatants were  
544 combined and 0.1 µg Trypsin was added followed by overnight incubation at RT. The  
545 digestion was stopped by adding TFA (final concentration 0.5%). The resulting  
546 digested samples were desalted and purified using StageTips (50). The peptides  
547 were eluted from StageTips with buffer B (80% acetonitrile, 0.1% formic acid),  
548 concentrated to 5 µL by SpeedVac centrifugation at room temperature, and filled up  
549 to 12 µL using buffer A (0.1% formic acid). Pulldown samples were measured using  
550 a gradient from 9-32% Buffer B for 114 minutes followed by washes at 50% then  
551 95% Buffer B, resulting in total 140 minutes data collection time. Mass spectra were  
552 recorded on an LTQ-Orbitrap Fusion Tribrid mass spectrometer (Thermo Fisher



553 Scientific). Scans were collected in data-dependent top speed mode with dynamic  
554 exclusion set at 60 seconds.

### 555 **Mass spectrometry analysis**

556 Thermo RAW files were analyzed with MaxQuant version 1.5.1.0 using default  
557 parameters. Searches were performed against the Uniprot mouse proteome,  
558 downloaded at June 2017. Additional parameters that were enabled were match-  
559 between-runs, label-free quantification (LFQ) and IBAQ. After filtering for proteins  
560 that were present at least in all replicates of one condition, LFQ values were log2  
561 transformed and missing values were imputed in Perseus using default parameters  
562 (width = 0.3, shift = 1.8). Statistical outliers for the pulldowns were determined using  
563 a two-tailed *t*-test. Multiple testing correction was performed using a permutation-  
564 based false discovery rate (FDR) method in Perseus. Volcano plots and  
565 stoichiometry calculations were performed as described previously (51).

566

567 **Chromatin immunoprecipitation:** Cells for H3K27Ac and RNAPII ChIPs were fixed  
568 using 1% formaldehyde at room temperature for 10 mins. Formaldehyde crosslinking  
569 was quenched by adding Glycine to a final concentration of 0.125M directly to the  
570 fixation solution, followed by an additional 5 min incubation at room temperature.  
571 Cells for anti-HA (BRD9/SS18-SSX1) ChIPs were subjected to a 2-stage fixation;  
572 cells were initially fixed for 30 mins at room temperature using 0.5mM DSG, followed  
573 by an additional 10 mins at room temperature using 1% formaldehyde.  
574 Formaldehyde crosslinking was quenched as outlined above. Fixed cells were  
575 washed 2X with ice-cold PBS and pelleted by centrifugation. Nuclei were extracted  
576 by resuspending fixed cell pellets in LB1 buffer (50mM HEPES, 140mM NaCl, 1mM  
577 EDTA, 10% Glycerol, 0.5% NP40, 0.25% Triton X100) containing 1X protease  
578 inhibitor cocktail (Biotools, B14002), followed by 10 mins incubation. Cells were  
579 pelleted by centrifugation and resuspended in LB2 buffer (10mM Tris pH8.0, 200mM  
580 NaCl, 1mM EDTA, 0.5mM EGTA) containing 1X protease inhibitor cocktail. Extracted  
581 nuclei were lysed using Covaris shearing buffer (0.1% SDS, 1mM EDTA and 10mM  
582 Tris pH 8.0) containing 1X protease inhibitor cocktail. Nuclei were lysed at a  
583 concentration of 10-30 million cells/ml in shearing buffer and sonicated in a Covaris  
584 E220, 1ml AFA milltubes (with fiber), Water level = 5, Duty Cycle = 5%, Peak  
585 Incidence Power = 140W, Cycle per burst = 200 for 16mins. Sonicated samples  
586 were pre-cleared by centrifugation at 14000rpm for 15mins at 4°C. A 0.25X volume

587 of 5X CHIP buffer (250 mM HEPES, 1.5 M NaCl, 5 mM EDTA pH 8.0, 5% Triton X-  
588 100, 0.5% DOC, and 0.5% SDS) was added to pre-cleared lysates, and these  
589 samples used directly for immunoprecipitations. For spike-in normalized CHIP  
590 experiments (CHIP-Rx) a 1:10 volume of fixed/sonicated chromatin derived for a  
591 mouse NIH3T3 cell line expressing a 3x HA epitope tagged BRD9 was added to  
592 each sample prior to the immunoprecipitation step.

593

594 **CHIP-seq library preparation and sequencing:** CHIP purified DNA was quantified  
595 using a Qubit fluorimeter (Invitrogen), and 2-50ng of DNA/CHIP was used to  
596 generate CHIP-seq libraries with the ThruPLEX DNA-seq kit (Rubicon Genomics,  
597 R400427). Library DNA was quantified using the Qubit, and size distributions were  
598 ascertained on a TapeStation (Agilent) using the D1000 ScreenTape assay reagents  
599 (Agilent, 5067-5583). This information was used to calculate pooling ratios for  
600 multiplex library sequencing. Pooled libraries were diluted and processed for 75bp  
601 single-end sequencing on an Illumina NextSeq instrument using the NextSeq 500  
602 High Output v2 kit (75 cycle) (Illumina, FC-404-2005) in accordance with the  
603 manufacturer's instructions.

604

605 **Cell count RNA-seq library prep and sequencing:** Total RNA was isolated from  
606 cells using the RNeasy Mini Kit (Qiagen, 74106) in accordance with the  
607 manufacturer's instructions. ERCC spike-in controls were added to isolated RNA to  
608 facilitate cell count normalization of RNA-sequencing data. The quality of extracted  
609 RNA was confirmed using a Bioanalyzer (Agilent) and 1 $\mu$ g of total RNA was  
610 used/sample as library prep input. Libraries were generated using the NEBNext Ultra  
611 RNA Library Prep kit for Illumina (NEB, E7530L) in accordance with the  
612 manufacturer's instructions. Library DNA was quantified using the Qubit, and size  
613 distributions were ascertained on a TapeStation (Agilent) using the D1000  
614 ScreenTape assay reagents (Agilent, 5067-5583). This information was used to  
615 calculate pooling ratios for multiplex library sequencing. Pooled libraries were diluted  
616 and processed for 75bp single-end sequencing on an Illumina NextSeq instrument  
617 using the NextSeq 500 High Output v2 kit (75 cycle) (Illumina, FC-404-2005) in  
618 accordance with the manufacturer's instructions.

619

620 **ChIP and RNA-seq data analysis:**

621 ChIP-seq analysis was performed using pipelines on the omics analysis platform  
622 Basepair (<http://www.basepair.io>). ChIP fastq files were trimmed to remove adapter  
623 and low quality sequences using trim\_galore and aligned to the UCSC genome  
624 assembly hg19 using Bowtie (version 2.1.0). For spike-in normalized ChIP-seq  
625 experiments reads were separately aligned to hg19 and mm9 using Bowtie.  
626 Duplicate reads were removed using Picard Mark Duplicates. Peaks were detected  
627 using MACS (version 1.4) using a p value cutoff was set to  $10^{-5}$ . Peaks were  
628 annotated to genomic features (Promoter, Gene body, Intergenic) using custom  
629 scripts on the Basepair platform, based on the UCSC database for hg19. ChIP-seq  
630 data visualisations were generated using the EaSeq analysis software (52).

631  
632 RNA-seq fastq files were aligned to NCBI37/hg19 and normalized using STAR.  
633 Differential expression data were obtained using the DEseq algorithm. These  
634 analyses were all done through the Basepair analysis platform  
635 (<http://www.basepair.io>).

636  
637 **Immunoblotting:** Whole cell protein samples were prepared in RIPA buffer (25mM  
638 Tris-HCl, pH7.6, 150mM NaCl, 1% NP-40, 1% Sodium Deoxycholate, 0.1% SDS)  
639 containing 1X protease inhibitor cocktails. Protein lysates were separated on pre-  
640 cast Bolt 4-12% Bis-Tris Plus Gels (Invitrogen, NW04127BOX) and transferred to  
641 nitrocellulose membranes. Membranes were subsequently probed using the relevant  
642 primary and secondary antibodies and relative protein levels were determined using  
643 the Odyssey CLx Imager (LI-COR).

644  
645 **Cellular viability, cell cycle and apoptosis analysis:** For dose response viability  
646 assays, cells were plated in 96-well tissue culture plates (1000 cells/well) in media  
647 containing DMSO or the desired concentration of each compound. Media was  
648 changed every 3-days up to a total of 9-days, at which point the ATPlite 1-Step  
649 luminescence assay system (PerkinElmer, 6016731) was used to determine ATP-  
650 dependent luminescence as an approximation of cellular viability. For cell cycle and  
651 apoptosis analysis cells were initially seeded on 10cm dishes in media containing  
652 DMSO or 100nM dBRD9-A and cultured/passaged in this media for a total of 9 days.  
653 For cell cycle analysis control and treated cells were harvested at 3/6/9 days and

654 processed for FACs analysis using the BD Pharmingen BrdU Flow kit (BD, 559619)  
655 in accordance with the manufacturer's instructions. For apoptosis analysis cells were  
656 harvested at 3/6/9 days (using Accutase to maintain cell membrane integrity) and  
657 processed for FACs analysis using the BD Annexin V Apoptosis Detection kit (BD,  
658 556547) in accordance with the manufacturer's instructions. Stained cells were  
659 analysed on a BD LSRFortessa Cell Analyzer and data processed using FlowJo  
660 software.

661

662 **Mouse experiments:** 4-6 week old female BALB/c (*Foxn1<sup>nu</sup>*) were purchased from  
663 Charles River Laboratories. For xenograft experiments mice were subcutaneously  
664 injected with 5 million synovial sarcoma cells in a 50/50 mix of culture  
665 media/matrigel. For treatment experiments dBRD9-A (50mg/kg) was administered  
666 once daily via intraperitoneal injection, over a total of 24 days. All experiments  
667 described were approved by and adhered to the guidelines of the Dana Farber  
668 Cancer Institute animal care and use committee.

669

#### 670 **Antibodies:**

671 **Antibodies used for Western blotting:** rabbit anti-BRD9 polyclonal, Bethyl Labs  
672 (catalogue number: A303-781A), rabbit anti-HA monoclonal, Cell Signaling  
673 Technology (catalogue number: 3724S), mouse anti-ACTIN monoclonal, Cell  
674 Signaling Technology (catalogue number: 3700S), rabbit anti-CRBN polyclonal,  
675 Proteintech (catalogue number: 11435-1-AP), rabbit anti-V5 polyclonal, Bethyl Labs  
676 (catalogue number: A190-220A). Goat anti-Rabbit IgG polyclonal, LI-COR (catalogue  
677 number: 925-32211) and goat anti-Mouse IgG polyclonal, LI-COR (catalogue  
678 number: 926-68070).

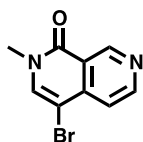
679 **Antibodies used for IP:** mouse anti-HA monoclonal magnetic beads, Pierce  
680 (catalogue number: 88837), mouse anti-V5 monoclonal agarose beads, Sigma  
681 (catalogue number: A7345-1ML), rabbit anti-BRD9 polyclonal, Bethyl Labs  
682 (catalogue number: A303-781A), rabbit anti-SSX1 polyclonal, MyBiosource  
683 (catalogue number: MBS9408371), rabbit anti-SSX2 polyclonal, MyBiosource  
684 (catalogue number: MBS9127222).

685

686 **Antibodies used for ChIP:** rabbit anti-HA monoclonal, Cell Signaling Technology  
687 (catalogue number: 3724S), rabbit anti-H3K27Ac polyclonal, Abcam (catalogue  
688 number: ab4729), mouse anti-RNAPII monoclonal, Diagenode (catalogue number:  
689 C15100055-100).

690

#### 691 **Chemical synthesis of dBRD9-A**



692

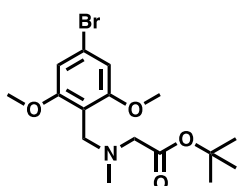
#### 693 **4-bromo-2-methyl-2,7-naphthyridin-1(2H)-one**

694 To a fine suspension of 4-bromo-2-methyl-2,7-naphthyridin-1(2H)-one (996 mg, 4.43  
695 mmol, 1.0 eq) and Cesium Carbonate (4330 mg, 13.3 mmol, 3.0 eq) in THF (17.7  
696 mL) was added Iodomethane (551  $\mu$ L, 8.86 mmol, 2.0 eq) and stirred at RT. After  
697 22hrs, the mixture was concentrated in vacuo, and the resulting residue dissolved in  
698 DCM. Insoluble material was filtered and washed with both DCM and water before  
699 being discarded. Organic filtrate was collected (approx. 150mL), washed three times  
700 with deionized water (30 mL), and finally with saturated brine (30 millileters), before  
701 being dried over Na<sub>2</sub>SO<sub>4</sub> and concentrated in vacuo to give the desired product as  
702 an off-white solid (1038 mg, 98%).

703 **<sup>1</sup>H NMR** <sup>1</sup>H NMR (500 MHz, DMSO-*d*<sub>6</sub>)  $\delta$  = 9.36 (s, 1H), 8.88 (s, 1H), 8.25 (s, 1H),  
704 7.61 (s, 1H), 3.54 (s, 3H).

705 **LCMS:** 239 (M).

706



707

#### 708 **tert-butyl 2-((4-bromo-2,6-dimethoxybenzyl)(methyl)amino)acetate**

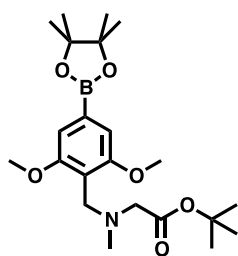
709 Sarcosyl tert-butyl ester hydrochloride (556 mg, 3.06 mmol, 1.5 eq) was dissolved in  
710 a solution of NaOAc (251 mg, 3.06 mmol, 1.5 eq), in DCM (8.2 mL), before 167  $\mu$ L  
711 AcOH (2.04 mmol, 1.0 eq) was added, followed by 4-bromo-2,6-  
712 dimethoxybenzaldehyde (500 mg, 2.04 mmol, 1.0 eq). The mixture was stirred for 10  
713 min before sodium triacetoxy borohydride was added in one portion (864.8 mg, 4.08  
714 mmol, 2.0 eq), and the mixture stirred for 18hr. The reaction was basified to

715 approximately pH 11 with 1M K<sub>2</sub>CO<sub>3</sub> and extracted 4 times with DCM (10 mL). The  
716 combined organics were washed with deionized water (10 mL), and saturated brine  
717 (10 mL), before being dried over Na<sub>2</sub>SO<sub>4</sub> and concentrated in vacuo to give the  
718 desired product as an off-white solid (725 mg, 95%).

719 <sup>1</sup>H NMR (500 MHz, Chloroform-*d*) δ = 6.69 (s, 2H), 3.81 (s, 2H), 3.79 (s, 6H), 3.21  
720 (s, 2H), 2.41 (s, 3H), 1.48 (s, 9H).

721 **LCMS:** 376 (M+H).

722



723

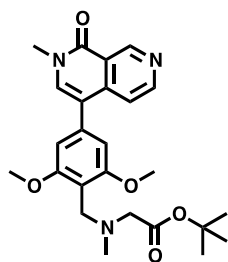
724 *tert*-butyl 2-((2,6-dimethoxy-4-(4,4,5,5-tetramethyl-1,3,2-dioxaborolan-2-  
725 yl)benzyl)(methyl)amino)acetate

726 *tert*-butyl 2-((4-bromo-2,6-dimethoxybenzyl)(methyl)amino)acetate (300 mg, 0.802  
727 mmol, 1.0 eq) and bis(pinacolato)diboron (305mg, 1.20 mmol, 1.5 eq), were  
728 dissolved in DMF, before KOAC (394 mg, 4.01 mmol, 5.0 eq), and PdCl<sub>2</sub>(dppf) •  
729 CH<sub>2</sub>Cl<sub>2</sub> (65.5 mg, 0.080 mmol, 0.1 eq) were added. The mixture was degassed, and  
730 headspace flushed with N<sub>2</sub> before heating to 90°C for 16hr. The reaction was diluted  
731 to 80 mL with EtOAc, filtered through celite, and washed twice with a 1:1 solution of  
732 deionized water and saturated brine (20 mL), three times with deionized water (20  
733 mL), and once with saturated brine (20 mL), before being dried over Na<sub>2</sub>SO<sub>4</sub> and  
734 concentrated in vacuo. The residue was dissolved in DCM and purified by silica  
735 chromatography (EtOAc/Hexanes 0 to 100% gradient) to give the desired product as  
736 a brown solid (158 mg, 47%).

737 <sup>1</sup>H NMR: (500 MHz, Chloroform-*d*) δ = 6.98 (s, 2H), 3.90 (s, 2H), 3.85 (s, 6H), 3.20  
738 (s, 2H), 2.41 (s, 3H), 1.48 (s, 9H), 1.35 (s, 12H).

739 **LCMS:** 423 (M+H).

740

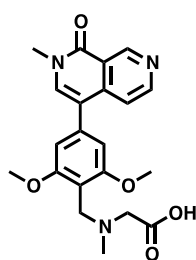


741  
 742 **tert-butyl 2-((2,6-dimethoxy-4-(2-methyl-1-oxo-1,2-dihydro-2,7-naphthyridin-4-**  
 743 **yl)benzyl)(methylamino)acetate**

744 4-bromo-2-methyl-2,7-naphthyridin-1(2H)-one (476 mg, 2.0 mmol, 1.0 eq) and tert-  
 745 butyl 2-((2,6-dimethoxy-4-(4,4,5,5-tetramethyl-1,3,2-dioxaborolan-2-  
 746 yl)benzyl)(methylamino)acetate (1.01 g, 2.4 mmol, 1.2 eq) (prepared over multiple  
 747 batches as above) were dissolved in DMF (10 mL) before a 2N solution of Na<sub>2</sub>CO<sub>3</sub>  
 748 was added (2.5 mL, 5 mmol, 2.5 eq) followed by Pd(dppf)Cl<sub>2</sub> • DCM (366 mg, 0.2  
 749 mmol, 0.1 eq). The mixture was degassed and heated to 80°C overnight. Solvent  
 750 was removed by lyophilization and the crude product was used directly.

751 **LCMS:** 454 (M + H).

752



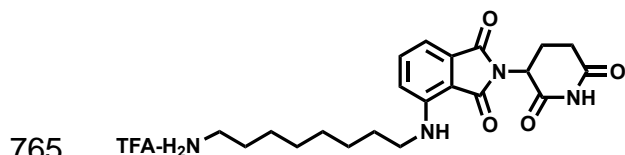
753  
 754 **2-((2,6-dimethoxy-4-(2-methyl-1-oxo-1,2-dihydro-2,7-naphthyridin-4-**  
 755 **yl)benzyl)(methylamino)acetic acid**

756 The above residue was dissolved in DCM (2 mL) before TFA (2 mL) was slowly  
 757 added. After stirring at rt for 24 hours, the mixture was concentrated in vacuo. The  
 758 residue was purified by prep-HPLC (0.05 % TFA) to give the desired product as an  
 759 off-white solid (410 mg, 51 % over 2 steps)

760 **<sup>1</sup>H NMR** (500 MHz, DMSO-d<sub>6</sub>) δ = 9.76 (s, 1H), 9.48 (s, 1H), 8.75 (d, 1H), 7.94 (s,  
 761 1H), 7.64 (d, 1H), 6.87 (s, 2H), 4.42 (s, 2H), 4.02 (s, 2H), 3.87 (s, 6H), 3.63 (s, 3H),  
 762 2.76 (s, 3H).

763 **LCMS:** 398 (M+H).

764



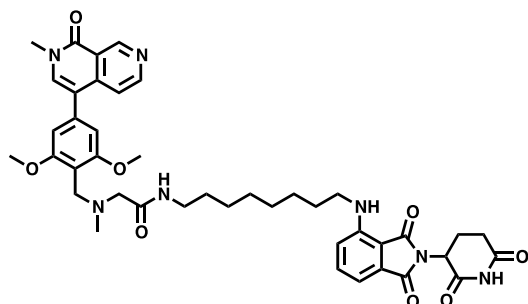
766 **4-((8-aminooctyl)amino)-2-(2,6-dioxopiperidin-3-yl)isoindoline-1,3-dione (4):**

767 To a solution of 2-(2,6-dioxopiperidin-3-yl)-4-fluoroisoindoline-1,3-dione (800 mg, 2.9  
768 mmol) and tert-butyl (8-aminooctyl)carbamate (710 mg, 2.9 mmol) in NMP (15 mL,  
769 0.2 M) was added DIPEA (451 mg, 3.5 mmol). The mixture was stirred at 90°C  
770 overnight, cooled to room temperature, diluted with EtOAc (100 mL), and washed  
771 with water (3 x 50 mL). The organic phase was washed with brine (50 mL), dried  
772 over anhydrous Na<sub>2</sub>SO<sub>4</sub>, and filtered. The filtrate was concentrated in vacuo, and  
773 the residue was stirred in TFA / CH<sub>2</sub>Cl<sub>2</sub> (2 mL / 4 mL) for 2 hours at rt. The volatile  
774 was removed and the residue was purified by prep-HPLC (0.05 % TFA in CH<sub>3</sub>CN /  
775 H<sub>2</sub>O) to afford the desired product (687 mg, 46 %) as a yellow solid.

776 **<sup>1</sup>H NMR** (500 MHz, Methanol-d<sub>4</sub>) δ 7.59 – 7.51 (m, 1H), 7.04 (dd, J = 7.9, 1.7 Hz,  
777 2H), 5.06 (dd, J = 12.4, 5.5 Hz, 1H), 3.34 (d, J = 7.0 Hz, 2H), 2.95 – 2.81 (m, 3H),  
778 2.79 – 2.66 (m, 2H), 2.15 – 2.08 (m, 1H), 1.67 (tt, J = 12.2, 7.2 Hz, 4H), 1.43 (d, J =  
779 22.2 Hz, 8H).

780 **LCMS** 401.39 (M+H).

781



782

783 **dBRD9-A**

784 To a solution of 4-((8-aminooctyl)amino)-2-(2,6-dioxopiperidin-3-yl)isoindoline-1,3-  
785 dione trifluoroacetate salt (669 mg, 1.3 mmol) and 2-((2,6-dimethoxy-4-(2-methyl-1-  
786 oxo-1,2-dihydro-2,7-naphthyridin-4-yl)benzyl)(methyl)amino)acetic acid (520 mg, 1.3  
787 mmol) in DMF (5 mL) was added HATU (990 mg, 2.6 mmol) and DIPEA (516 mg, 4  
788 mmol). The mixture was stirred at rt. for 2 hours, diluted with ethyl acetate (50 mL),  
789 and washed with water (3 x 20 mL) and brine (20 mL), dried over anhydrous



790 Na<sub>2</sub>SO<sub>4</sub>, filtered and concentrated. The residue was purified by prep-HPLC (0.05 %  
791 TFA in CH<sub>3</sub>CN / H<sub>2</sub>O) to afford **dBRD9-A** (583 mg, 50 %) as a yellow solid.

792 <sup>1</sup>H NMR (500 MHz, Methanol-*d*<sub>4</sub>) δ 9.54 (s, 1H), 8.67 (d, *J* = 6.1 Hz, 1H), 7.89 (s,  
793 1H), 7.77 (d, *J* = 6.0 Hz, 1H), 7.51 (dd, *J* = 8.5, 7.2 Hz, 1H), 6.99 (dd, *J* = 7.8, 2.2 Hz,  
794 2H), 6.84 (s, 2H), 5.48 (s, 2H), 5.03 (dd, *J* = 12.6, 5.5 Hz, 1H), 4.51 (d, *J* = 4.9 Hz,  
795 2H), 3.95 (s, 6H), 3.70 (s, 3H), 3.34 (s, 1H), 3.27 (t, *J* = 6.9 Hz, 2H), 2.92 (s, 3H),  
796 2.85 (ddd, *J* = 17.5, 13.9, 5.2 Hz, 1H), 2.76 – 2.65 (m, 2H), 2.13 – 2.06 (m, 1H), 1.61  
797 (p, *J* = 6.9 Hz, 2H), 1.52 – 1.46 (m, 2H), 1.43 – 1.25 (m, 11H).

798 **LCMS:** 780.9 (M+H).

799

### 800 **Accession numbers**

801 All next-generation sequencing datasets generated in association with this work  
802 have been deposited in the Gene Expression Omnibus (GEO) under accession  
803 number GSE113229  
804 (<https://www.ncbi.nlm.nih.gov/geo/query/acc.cgi?acc=GSE113229>). For review  
805 purposes please use reviewers token - avibugkwdbjfyf - to access the data.

806

### 807 **Acknowledgements**

808 We thank members of the Armstrong, Vakoc and Bradner laboratories for engaging  
809 discussions throughout the course of this work. We thank B. Knoechel, R. Isenhardt,  
810 S. Potdar and J. Kloeber for assistance with next-generation sequencing  
811 experiments. We thank X. Wang for technical assistance in relation to chromatin  
812 immunoprecipitation experiments. This work was supported by grants from the NCI  
813 (CA176745, CA066996, CA204915) and Alex's Lemonade Stand Foundation to  
814 S.A.A. G.L.B. was supported by an EMBO Long-Term Fellowship (ALTF-1235-2015)  
815 and an Irish Cancer Society Biomedical Research Fellowship (CRF18BRI). S.A.A. is  
816 a consultant and/or shareholder for Imago Biosciences, Cyteir Therapeutics, C4  
817 Therapeutics, Syros Pharmaceuticals, OxStem Oncology, ProQR and Accent  
818 Therapeutics. S.A.A. receives research support from Janssen, Novartis, and  
819 AstraZeneca.

820

### 821 **Author Contributions**

822 G.L.B, J.S, C.R.V and S.A.A conceived the study. G.L.B performed most of the  
823 experiments, D.R synthesized and contributed to applications of dBRD9-A, J.S

824 generated the custom sgRNA libraries and performed next-generation sequencing  
825 related to CRISPR screening experiments, M.L.H assisted with bioinformatics  
826 analysis of ChIP and RNA-seq experiments, K.W, E.T.D, and G.C performed mass  
827 spec analysis, J.Q, S.F and J.E.B contributed cell lines and reagents. G.L.B and  
828 S.A.A interpreted experimental results and G.L.B wrote the manuscript with  
829 contributions from all authors.

830

831

832

833

834

835

836

837

### 838 **References**

- 839 1. Z. Burningham, M. Hashibe, L. Spector, J. D. Schiffman, The Epidemiology of  
840 Sarcoma. *Clin. Sarcoma Res.* **2**, 14 (2012).
- 841 2. J. L. Anderson, C. T. Denny, W. D. Tap, N. Federman, Pediatric sarcomas:  
842 translating molecular pathogenesis of disease to novel therapeutic  
843 possibilities. *Pediatr. Res.* **72**, 112–121 (2012).
- 844 3. Q. Gao *et al.*, Driver Fusions and Their Implications in the Development and  
845 Treatment of Human Cancers. *Cell Rep.* **23**, 227–238.e3 (2018).
- 846 4. A. S. Brohl *et al.*, The Genomic Landscape of the Ewing Sarcoma Family of  
847 Tumors Reveals Recurrent STAG2 Mutation. *PLoS Genet.* **10** (2014),  
848 doi:10.1371/journal.pgen.1004475.
- 849 5. F. Tirode *et al.*, Genomic landscape of ewing sarcoma defines an aggressive  
850 subtype with co-association of STAG2 and TP53 mutations. *Cancer Discov.* **4**,  
851 1342–1353 (2014).
- 852 6. B. D. Crompton *et al.*, The genomic landscape of pediatric Ewing sarcoma.  
853 *Cancer Discov.* **4**, 1326–1341 (2014).
- 854 7. M. Seki *et al.*, Integrated genetic and epigenetic analysis defines novel  
855 molecular subgroups in rhabdomyosarcoma. *Nat. Commun.* **6** (2015),  
856 doi:10.1038/ncomms8557.
- 857 8. J. F. Shern *et al.*, Comprehensive genomic analysis of rhabdomyosarcoma

- 858 reveals a landscape of alterations affecting a common genetic axis in fusion-  
859 positive and fusion-negative tumors. *Cancer Discov.* **4**, 216–231 (2014).
- 860 9. G. L. Brien, D. G. Valerio, S. A. Armstrong, Exploiting the Epigenome to  
861 Control Cancer-Promoting Gene-Expression Programs. *Cancer Cell.* **29**, 464–  
862 476 (2016).
- 863 10. J. Clark *et al.*, Identification of novel genes, SYT and SSX, involved in the  
864 t(X;18)(p11.2;q11.2) translocation found in human synovial sarcoma. *Nat.*  
865 *Genet.* **7**, 502–508 (1994).
- 866 11. B. De Leeuw, M. Balemans, D. O. Weghuis, A. G. Van Kessel, Identification of  
867 two alternative fusion genes, SYT-SSX1 and SYT-SSX2, in t(X;  
868 18)(p11.2;q11.2)-positive synovial sarcomas. *Hum. Mol. Genet.* **4**, 1097–  
869 1099 (1995).
- 870 12. B. Skytting *et al.*, A Novel Fusion Gene , SYT – SSX4 , in Synovial Sarcoma  
871 fusion messenger RNA in biopsy speci-. **91**, 4–5 (1999).
- 872 13. A. Abeshouse *et al.*, Comprehensive and Integrated Genomic Characterization  
873 of Adult Soft Tissue Sarcomas. *Cell.* **171**, 950–965.e28 (2017).
- 874 14. J. Barretina *et al.*, Subtype-specific genomic alterations define new targets for  
875 soft-tissue sarcoma therapy. *Nat. Genet.* **42**, 715–721 (2010).
- 876 15. M. Haldar, J. D. Hancock, C. M. Coffin, S. L. Lessnick, M. R. Capecchi, A  
877 Conditional Mouse Model of Synovial Sarcoma: Insights into a Myogenic  
878 Origin. *Cancer Cell.* **11**, 375–388 (2007).
- 879 16. E. Middeljans *et al.*, SS18 together with animal-specific factors defines human  
880 BAF-type SWI/SNF complexes. *PLoS One.* **7** (2012),  
881 doi:10.1371/journal.pone.0033834.
- 882 17. C. Kadoch, G. R. Crabtree, Reversible disruption of mSWI/SNF (BAF)  
883 complexes by the SS18-SSX oncogenic fusion in synovial sarcoma. *Cell.* **153**  
884 (2013), pp. 71–85.
- 885 18. F. L. Lim, M. Soulez, D. Koczan, H.-J. Thiesen, J. C. Knight, A KRAB-related  
886 domain and a novel transcription repression domain in proteins encoded by  
887 SSX genes that are disrupted in human sarcomas. *Oncogene.* **17**, 2013–2018  
888 (1998).
- 889 19. M. Soulez, A. J. Saurin, P. S. Freemont, J. C. Knight, SSX and the synovial-  
890 sarcoma-specific chimaeric protein SYT-SSX co-localize with the human  
891 Polycomb group complex. *Oncogene.* **18**, 2739–2746 (1999).

- 892 20. M. J. McBride *et al.*, The SS18-SSX Fusion Oncoprotein Hijacks BAF Complex  
893 Targeting and Function to Drive Synovial Sarcoma. *Cancer Cell* (2018), ,  
894 doi:10.1016/j.ccell.2018.05.002.
- 895 21. A. Banito *et al.*, The SS18-SSX Oncoprotein Hijacks KDM2B-PRC1.1 to Drive  
896 Synovial Sarcoma. *Cancer Cell*. **33**, 527–541.e8 (2018).
- 897 22. L. Su *et al.*, Deconstruction of the SS18-SSX Fusion Oncoprotein Complex:  
898 Insights into Disease Etiology and Therapeutics. *Cancer Cell*. **21**, 333–347  
899 (2012).
- 900 23. C. Kadoch *et al.*, Dynamics of BAF–Polycomb complex opposition on  
901 heterochromatin in normal and oncogenic states. *Nat. Genet.* **49**, 213–222  
902 (2016).
- 903 24. J. Shi *et al.*, Discovery of cancer drug targets by CRISPR-Cas9 screening of  
904 protein domains. *Nat. Biotechnol.*, 1–10 (2015).
- 905 25. J. Shi, C. R. Vakoc, The Mechanisms behind the Therapeutic Activity of BET  
906 Bromodomain Inhibition. *Mol. Cell*. **54**, 72–736 (2014).
- 907 26. T. Hensel *et al.*, Targeting the EWS-ETS transcriptional program by BET  
908 bromodomain inhibition in Ewing sarcoma. *Oncotarget*. **7**, 1451–63 (2016).
- 909 27. E. R. McDonald *et al.*, Project DRIVE: A Compendium of Cancer  
910 Dependencies and Synthetic Lethal Relationships Uncovered by Large-Scale,  
911 Deep RNAi Screening. *Cell*. **170**, 577–592.e10 (2017).
- 912 28. C. Kadoch *et al.*, Proteomic and bioinformatic analysis of mammalian  
913 SWI/SNF complexes identifies extensive roles in human malignancy. *Nat.*  
914 *Genet.* **45**, 592–601 (2013).
- 915 29. A. Alpsy, E. C. Dykhuizen, Glioma tumor suppressor candidate region gene 1  
916 (GLTSCR1) and its paralog GLTSCR1-like form SWI/SNF chromatin  
917 remodeling subcomplexes. *J. Biol. Chem.* (2018),  
918 doi:10.1074/jbc.RA117.001065.
- 919 30. B. Schwanhausser *et al.*, Global quantification of mammalian gene expression  
920 control. *Nature*. **473**, 337–342 (2011).
- 921 31. D. Savic *et al.*, CETCh-seq: CRISPR epitope tagging ChIP-seq of DNA-binding  
922 proteins. *Genome Res.* **25**, 1581–1589 (2015).
- 923 32. A. F. Hohmann *et al.*, Sensitivity and engineered resistance of myeloid  
924 leukemia cells to BRD9 inhibition. *Nat. Chem. Biol.* **12**, 672–9 (2016).
- 925 33. L. J. Martin *et al.*, Structure-Based Design of an in Vivo Active Selective BRD9

- 926 Inhibitor. *J. Med. Chem.* **59**, 4462–4475 (2016).
- 927 34. N. H. Theodoulou *et al.*, Discovery of I-BRD9, a Selective Cell Active Chemical  
928 Probe for Bromodomain Containing Protein 9 Inhibition. *J. Med. Chem.* **59**,  
929 1425–1439 (2016).
- 930 35. D. Remillard *et al.*, Degradation of the BAF Complex Factor BRD9 by  
931 Heterobifunctional Ligands. *Angew Chem Int Ed Engl.* **56**, 5738–5743 (2017).
- 932 36. D. Hnisz *et al.*, Super-enhancers in the control of cell identity and disease.  
933 *Cell.* **155**, 934–47 (2013).
- 934 37. J. Lovén *et al.*, Selective inhibition of tumor oncogenes by disruption of super-  
935 enhancers. *Cell.* **153**, 320–334 (2013).
- 936 38. K. W. Lee, N. K. Lee, S. Ham, T. Y. Roh, S. H. Kim, Twist1 is essential in  
937 maintaining mesenchymal state and tumor-initiating properties in synovial  
938 sarcoma. *Cancer Lett.* **343**, 62–73 (2014).
- 939 39. P. Francis *et al.*, Diagnostic and prognostic gene expression signatures in 177  
940 soft tissue sarcomas: hypoxia-induced transcription profile signifies metastatic  
941 potential. *BMC Genomics.* **8**, 73 (2007).
- 942 40. A. E. Sarver, A. L. Sarver, V. Thayanithy, S. Subramanian, Identification, by  
943 systematic RNA sequencing, of novel candidate biomarkers and therapeutic  
944 targets in human soft tissue tumors. *Lab. Invest.* **95**, 1077–88 (2015).
- 945 41. J. Terry *et al.*, TLE1 as a diagnostic immunohistochemical marker for synovial  
946 sarcoma emerging from gene expression profiling studies. *Am. J. Surg. Pathol.*  
947 **31**, 240–6 (2007).
- 948 42. A. Takahashi *et al.*, Analysis of gene expression profiles of soft tissue sarcoma  
949 using a combination of knowledge-based filtering with integration of multiple  
950 statistics. *PLoS One.* **9** (2014), doi:10.1371/journal.pone.0106801.
- 951 43. K. Baird *et al.*, Gene expression profiling of human sarcomas: Insights into  
952 sarcoma biology. *Cancer Res.* **65**, 9226–9235 (2005).
- 953 44. K. F. Krämer, N. Moreno, M. C. Frühwald, K. Kerl, BRD9 inhibition, alone or in  
954 combination with cytostatic compounds as a therapeutic approach in rhabdoid  
955 tumors. *Int. J. Mol. Sci.* **18** (2017), doi:10.3390/ijms18071537.
- 956 45. M. H. Bailey *et al.*, Comprehensive Characterization of Cancer Driver Genes  
957 and Mutations. *Cell.* **173**, 371–385.e18 (2018).
- 958 46. S. F. Cai, C.-W. Chen, S. A. Armstrong, Drugging Chromatin in Cancer:  
959 Recent Advances and Novel Approaches. *Mol. Cell.* **60**, 561–570 (2015).

- 960 47. G. L. Brien *et al.*, A chromatin-independent role of polycomb-like 1 to stabilize  
961 p53 and promote cellular quiescence. *Genes Dev.* **29**, 2231–2243 (2015).
- 962 48. J. R. Wisniewski, A. Zougman, N. Nagaraj, M. Mann, J. R. Wi, Universal  
963 sample preparation method for proteome analysis. *Nat. Methods.* **6**, 377–362  
964 (2009).
- 965 49. J. Cox, M. Mann, MaxQuant enables high peptide identification rates,  
966 individualized p.p.b.-range mass accuracies and proteome-wide protein  
967 quantification. *Nat Biotechnol.* **26**, 1367–1372 (2008).
- 968 50. J. Rappsilber, M. Mann, Y. Ishihama, Protocol for micro-purification,  
969 enrichment, pre-fractionation and storage of peptides for proteomics using  
970 StageTips. *Nat. Protoc.* (2007), doi:10.1038/nprot.2007.261.
- 971 51. A. H. Smits, P. W. T. C. Jansen, I. Poser, A. a. Hyman, M. Vermeulen,  
972 Stoichiometry of chromatin-associated protein complexes revealed by label-  
973 free quantitative mass spectrometry-based proteomics. *Nucleic Acids Res.* **41**,  
974 1–8 (2013).
- 975 52. M. Lerdrup, J. V. Johansen, S. Agrawal-Singh, K. Hansen, An interactive  
976 environment for agile analysis and visualization of ChIP-sequencing data. *Nat.*  
977 *Struct. Mol. Biol.* (2016), doi:10.1038/nsmb.3180.
- 978
- 979
- 980
- 981
- 982
- 983
- 984
- 985
- 986
- 987
- 988
- 989
- 990
- 991
- 992
- 993

994  
995  
996  
997  
998  
999  
1000  
1001  
1002  
1003  
1004  
1005  
1006  
1007  
1008  
1009  
1010  
1011  
1012  
1013  
1014  
1015  
1016  
1017  
1018  
1019  
1020  
1021  
1022  
1023  
1024  
1025  
1026  
1027

**Figure legends:**

**Figure 1: The BRD9 bromodomain is a functional dependency in synovial sarcoma**

- A.** Schematic representation of CRISPR/Cas9 based genomic screening approach.
- B.** Scatter plot representation of biological duplicate sgRNA screening data in synovial and Ewing’s sarcoma cell lines. Each dot denotes and individual sgRNA and axes represent  $\log_2$  fold-change in sgRNA abundance between day-3 and day-15. BRD9 bromodomain and control sgRNAs are highlighted.
- C.** Schematic representation of the BRD9 protein structure with sgRNA target sites indicated.
- D.** Negative selection based CRISPR-Cas9 mutagenesis assays. The relative GFP<sup>+</sup> (sgRNA<sup>+</sup>) subpopulation percentage is depicted at the indicated time-points after lentiviral infection. Mean +/- s.d., n = 3.
- E.** Waterfall plot representing “BRD9 sensitivity” score in a panel of cancer cell lines taken from the Project DRIVE database (ref. 18) (<https://oncology.nibr.shinyapps.io/drive/>).
- F.** Negative selection based CRISPR-Cas9 mutagenesis assays in bromodomain functional rescue experiments. The relative GFP<sup>+</sup> (sgRNA<sup>+</sup>) subpopulation percentage is depicted at the indicated time-points after lentiviral infection. Mean +/- s.d., n = 3.

1028

1029 **Figure 2: BRD9 functions as part of SS18-SSX containing SWI/SNF complexes**

1030 **A.** Silver stains of endogenous SS18-SSX fusion protein immunoprecipitations  
1031 performed on nuclear protein lysates prepared 2 independent synovial sarcoma cell  
1032 lines.

1033 **B.** Volcano plots representing fold enrichment (LFQ intensity) of proteins  
1034 identified by mass spec in SS18-SSX1 or SS18-SSX2 purifications relative to IgG  
1035 control purifications. Known BAF members are indicated in red.

1036 **C.** Western blots analyses of the indicated proteins performed on endogenous  
1037 BRD9 or IgG purifications in HSSYII cells (Input = 10% total IP material).

1038 **D.** Western blots analyses of the indicated proteins performed on endogenous  
1039 BRD9 or IgG purifications in SYO1 cells (Input = 10% total IP material).

1040 **E.** Scatter plot representing the normalized protein abundance (IBAQ score) of  
1041 proteins identified in SS18-SSX1 and SS18-SSX2 purifications. Known BAF  
1042 members are indicated in red

1043 **F.** High density sgRNA tiling of BRD9 in 2 independent SS cell lines. Each bar  
1044 represents the fold-change of an individual sgRNA and its target site along the BRD9  
1045 protein.

1046 **G.** Negative selection based CRISPR-Cas9 mutagenesis assays in amino acid  
1047 311-345 region functional rescue experiments. The relative GFP<sup>+</sup> (sgRNA<sup>+</sup>)  
1048 subpopulation percentage is depicted at the indicated time-points after lentiviral  
1049 infection. Mean +/- s.d., n = 3.

1050 **H.** Western blot analyses of the indicated proteins in anti-V5 purifications  
1051 performed in control HSSYII cells, or HSSYII cells expressing a full-length,  
1052 bromodomain deleted or amino acid 311-345 deleted BRD9.

1053

1054 **Figure 3: SS18-SSX1 and BRD9 co-bind the synovial sarcoma genome**

1055 **A.** Genomic tracks showing BRD9 and SS18-SSX1 ChIP-seq signal on the 98  
1056 Mb right arm of chromosome 8 in HSSYII cells. The chromosome 8 ideogram is  
1057 displayed above the gene tracks with the relevant region highlighted in red.

1058 **B.** Pie charts representing the distribution of BRD9 and SS18-SSX1 binding sites  
1059 on the synovial sarcoma genome.

1060 **C.** Venn diagram overlaps of all identified BRD9 and SS18-SSX1 ChIP-seq  
1061 peaks in HSSYII cells.



1062 **D.** Tornado plots showing BRD9, SS18-SSX1, RNAPII and H3K27Ac ChIP-  
1063 signal +/- 10kb of all hg19 gene promoters in HSSYII cells. Promoters are ranked by  
1064 RNAPII ChIP signal.

1065 **E.** Tornado plots showing BRD9, SS18-SSX1 and H3K27Ac ChIP-signal +/-  
1066 10kb of all active enhancers (defined by H327Ac) in HSSYII cells.

1067 **F.** Tracks showing BRD9 and SS18-SSX1 ChIP-seq occupancy at the indicated  
1068 genomic loci in HSSYII cells.

1069

1070 **Figure 4: Complete ablation of BRD9 function by targeted protein degradation**

1071 **A.** Cellular viability dose-response data in the indicated panel of cell lines treated  
1072 with the BRD9 bromodomain inhibitors BI7273 (top) or I-BRD9 (bottom). Mean +/-  
1073 s.d., n = 3.

1074 **B.** Tornado plots and meta-tracks representing BRD9 ChIP-Rx signal in control  
1075 (DMSO) and BI7273 treated (24hrs) HSSYII cells.

1076 **C.** ChIP-qPCR analysis of 3xHA epitope tagged full-length BRD9,  $\Delta$ 311-345  
1077 BRD9 or  $\Delta$  bromodomain BRD9 at the indicated gene promoters in HSSYII cells.  
1078 Mean +/- s.d., n = 3.

1079 **D.** Chemical structure of our BRD9 degrader compound dBRD9-A.

1080 **E.** Selectivity of phage-displayed bromodomain displacement by dBRD9-A  
1081 (Bromoscan).

1082 **F.** Western blot analysis of the indicated proteins, in 2 independent synovial  
1083 sarcoma cell lines following treatment with dBRD9-A at 100nM for 6-72h.

1084 **G.** Waterfall plot representing changes in BRD9 occupancy at BRD9 peak  
1085 regions in ChIP-Rx experiments of BI7273 (10 $\mu$ M) (left panel) or dBRD9-A (100nM)  
1086 (right panel) treated HSSYII cells following 24hrs treatment.

1087 **H.** Tracks showing BRD9 ChIP-seq occupancy on the 98 Mb right arm of  
1088 chromosome 8 after DMSO or 100nM dBRD9-A treatment. The chromosome 8  
1089 ideogram is displayed above the gene tracks with the relevant region highlighted in  
1090 red.

1091 **I.** Cellular viability dose-response data in HSSYII and SYO1 cells treated with  
1092 dBRD9-A or the BRD9 bromodomain inhibitors BI7273 or I-BRD9. Mean +/- s.d., n =  
1093 3.

1094

1095 **Figure 5: BRD9 degradation blocks synovial sarcoma tumour progression and**  
1096 **oncogenic transcription**

1097 **A.** Relative changes in cell cycle dynamics in 2 independent SS cell lines treated  
1098 with dBRD9-A for 3/6/9 days at 100nM. Mean +/- s.d., n = 3

1099 **B.** Relative changes in Annexin-V positive cells in 2 independent SS cell lines  
1100 treated with dBRD9-A for 3/6/9 days at 100nM. Mean +/- s.d., n = 3

1101 **C.** Tumour progression in a subcutaneous xenograft model of SS in control  
1102 vehicle treated mice, and mice treated at 50mg/kg dBRD9-A once daily for 24 days.  
1103 Mean +/- SEM, 5 mice per treatment group. P value is from 2way ANOVA

1104 **D.** Western blot analysis of the indicated proteins in protein lysates derived from  
1105 tumour tissue from 2 independent mice per treatment group as in panel c.

1106 **E.** Volcano plot representing gene expression changes in HSSYII cells treated  
1107 with dBRD9-A at 100nM for 6hrs. The number of genes, the expression of which  
1108 changes >1.5-fold up or down are indicated.

1109 **F.** H3K27Ac ChIP-seq signal (rpm/bp) at all enhancer regions in HSSYII cell.  
1110 Enhancers are ranked by increasing H3K27Ac signal.

1111 **G.** Box plot representations of changes in gene expression amongst genes  
1112 associated with typical enhancers and genes associated with super enhancers. P  
1113 values are from Welch's two-tailed t-tests. \*\*\*P≤0.001.

1114 **H.** Heat map representing changes in gene expression amongst all super  
1115 enhancer associated genes in HSSYII cells following 6hrs dBRD9-A treatment at  
1116 100nM, or HSSYII cells following infection with 2 independent SS18-SSX1 shRNAs  
1117 for 96hrs.

1118 **I.** Tracks showing BRD9 and SS18-SSX1 ChIP-seq occupancy at the indicated  
1119 genomic loci in DMSO and dBRD9-A treated cells. Also shown is H3K27Ac ChIP-  
1120 seq signal in untreated cells.

1121

1122 **Figure supplement legends:**

1123 **Figure 1-figure supplement 1: BRD9 is a specific functional dependency in**  
1124 **synovial sarcoma**

1125 **A.** Scatter plot representation of sgRNA screening data in synovial and Ewing's  
1126 sarcoma cell lines. Each dot denotes an individual bromodomain targeting sgRNA  
1127 and axes represent log<sub>2</sub> fold-change in sgRNA abundance between day-3 and day-  
1128 15. BRD4 and BRD9 bromodomain targeted sgRNAs are indicated. Highlighted

1129 region denotes sgRNAs depleted >2-fold in SS cells and unchanged in Ewing  
1130 sarcoma cells.

1131 **B.** Indel quantification by TIDE (Tracking of Indels by sequence trace  
1132 Decomposition) analysis 4 days after transduction with the indicated sgRNA in the  
1133 indicated cell lines. Also presented are GFP FACs plots collected at time of  
1134 harvesting, demonstrating the proportion of GFP+ (sgRNA+) cells in each instance.

1135 **C.** Western blot analysis of the indicated proteins in a cohort of synovial, and  
1136 non-synovial sarcoma cell lines.

1137 **D.** Western blot analysis of the indicated proteins in 4 independent SS cell lines  
1138 expressing a control shRNA (Renilla) or one of two independent BRD9 targeting  
1139 shRNAs.

1140 **E.** Negative selection-based shRNA functional assays in 4 independent SS cell  
1141 lines. The relative GFP+ (sgRNA+) subpopulation percentage is depicted at the  
1142 indicated time points after lentiviral infection. Mean +/- s.d., n = 3.

1143 **F.** Western blots (as in Panel c) in Ewing sarcoma (A673) and  
1144 rhabdomyosarcoma (RH30) cells lines.

1145 **G.** Negative selection-based shRNA assays (as in Panel e) in Ewing sarcoma  
1146 (A673) and rhabdomyosarcoma (RH30) cell lines.

1147 **H.** Schematic representation of the BRD9 coding region targeted by sgRNA-15.  
1148 The sgRNA target sequence is highlighted in red and PAM sequence is indicated  
1149 (top). The silent mutations added to render the allele insensitive to CRISPR/Cas9  
1150 targeting are indicated, and sequence of the CRISPR-resistant allele shown  
1151 (bottom).

1152 **I.** Western blot analysis of the indicated proteins in HSSYII cells used in function  
1153 rescue experiments.

1154

1155 **Figure 2-figure supplement 1: BRD9 is a component of SS18-SSX containing**  
1156 **BAF complexes.**

1157 **A.** Silver stains of anti-HA immunoprecipitations performed on nuclear protein  
1158 lysates prepared from HEK293T cell lines expression GFP (control) or an SS18-  
1159 SSX1 or SS18-SSX2 fusion protein.

1160 **B.** Volcano plots representing fold enrichment (LFQ intensity) of proteins  
1161 identified by mass spec in anti-HA-SS18-SSX1/2 purifications relative to GFP control  
1162 purifications. Known BAF members are indicated in red.

1163 **C.** Bar chart representing total peptide numbers identified for each of the  
1164 indicated BAF complex members in mass spec analysis of ant-HA-SS18-SSX1/2  
1165 purifications.

1166 **D.** Bar chart representing total peptide numbers identified for each of the  
1167 indicated BAF complex members in mass spec analysis of endogenous SS18-  
1168 SSX1/2 purifications.

1169 **E.** Bar chart representing the fold-change in abundance of individual sgRNAs  
1170 targeting the bromodomains of the indicated BAF members between day-15 and  
1171 day-3 of our functional genomics screening experiments.

1172

1173 **Figure 3-figure supplement 1: BRD9 and SS18-SSX1 co-localise genome-wide**

1174 **A.** Schematic representation of the CRISPR/Cas9 mediated targeting of a 3xHA  
1175 epitope tag to the C-termini of the BRD9 and SS18-SSX1 loci.

1176 **B.** Pie charts representing the proportion and total number of BRD9 and SS18-  
1177 SSX1 ChIP-seq peaks occurring in each of the 3 indicated genomic regions.

1178 **C.** Scatter plot representing the correlation of BRD9 and SS18-SSX1 ChIP-seq  
1179 signal within all identified BRD9 binding peaks.

1180 **D.** Venn diagram overlap of all BRD9 and SS18-SSX1 target genes identified in  
1181 this study, with SS18-SSX1 targets identified in the work of Banito et al.,(21).

1182

1183 **Figure 4-figure supplement 1: Transcriptional regulation by BRD9 in SS cells**

1184 **A.** Tornado plots showing BRD9-WT and BRD9-N216A ChIP-signal signal within  
1185 all BRD9 peaks regions. Regions are ranked by change in ChIP-signal (BRD9-  
1186 N216A/BRD9-WT).

1187 **B.** Genomic tracks showing BRD9-WT and BRD9-N216A ChIP-seq signal at the  
1188 indicated locus in HSSYII cells.

1189 **C.** Western blot analysis of the indicated proteins in wildtype or CRBN -/  
1190 HEK293T cells treated with 100nM dBRD9-A for 0, 24 or 48hrs.

1191 **D.** Western blot analysis of the indicated proteins in HSSYII cells treated with  
1192 increasing doses of dBRD9-A (100nM, 500nM) for 6h following pre-treatment of cells  
1193 for 12h with DMSO or BI7273 (5 $\mu$ M).

1194 **E.** Cellular viability dose-response data in SS (HSSYII and SYO1), Ewing  
1195 sarcoma (A673) and rhabdomyosarcoma (RH30) cell lines treated with dBRD9-A.

1196 Mean +/- s.d. n = 3.

1197 **F.** Western blot analysis of the indicated proteins in Ewing (A673) and  
1198 rhabdomyosarcoma (RH30) cell lines treated with dBRD9-A at 100nM for 6 to 72h.

1199 **G.** Western blot analyses of the indicated proteins in 2 independent synovial  
1200 sarcoma cell lines treated for the specified time course with BI7273 (left panels) at  
1201 5 $\mu$ M or dBRD9-A (right panels) at 100nM.

1202 **H.** Fold-change of all known BAF members identified by mass spectrometry in  
1203 SS18-SSX1 purifications performed in HSSYII cells treated with DMSO or dBRD9-A  
1204 for 24hrs.

1205

1206 **Figure 5-figure supplement 1: Targeted degradation of BRD9**

1207 **A.** Schematic representation of wildtype BRD9 and BRD7, and the chimeric  
1208 BRD9 bromodomain swap containing the BRD7 bromodomain (top panel). Western  
1209 blot analysis of the indicated proteins in HSSYII cells expressing vector (control),  
1210 BRD9-WT or BRD9 containing the bromodomain of BRD7 (BRD9-BD7) treated with  
1211 dBRD9-A at 100nM for 6h (bottom panel).

1212 **B.** Growth assays of HSSYII cells (as in panel a) cultured in the presence of  
1213 dBRD9-A at 100nM for a total of 9-days.

1214 **C.** Mouse weight measurements in vehicle control and dBRD9-A treated mice.  
1215 Mean +/- s.d., n = 5.

1216 **D.** Complete blood counts (CBCs) performed on vehicle control and dBRD9-A  
1217 treated mice. Measurements were taken on day-23 of the 24-day treatment  
1218 experiment. Mean +/- s.d., n = 5.

1219 **E.** Box plot representation of the relative abundance of BRD9 and SS18-SSX1  
1220 ChIP-seq signal at promoter, typical enhancer and super enhancer elements. P  
1221 values are from Welch's two-tailed t-tests. \*\*\* P  $\leq$ 0.001.

1222 **F.** Box plot representations of changes in SS18-SSX1 occupancy at active  
1223 promoters, typical enhancers and super enhancers comparing DMSO and dBRD9-A  
1224 treated HSSYII cells. P values are from Welch's two-tailed t-tests. \*P  $\leq$ 0.05,  
1225 \*\*\*P $\leq$ 0.001.

1226 **G.** Venn diagram representing the proportion of overlap between all up/down-  
1227 regulated genes (+/- 1.5-fold) in dBRD9-A treated cells at 6hrs post-treatment with all  
1228 direct SS18-SSX target genes.

1229  
1230  
1231  
1232  
1233  
1234  
1235  
1236  
1237  
1238  
1239  
1240  
1241  
1242  
1243  
1244  
1245  
1246  
1247  
1248  
1249  
1250  
1251  
1252  
1253  
1254  
1255  
1256  
1257  
1258  
1259  
1260  
1261  
1262

**Source data:**

**Figure 1:**

**Figure 1-source data 1:** Sequencing read counts and fold-change values for individual sgRNAs in library experiments in HSSYII synovial sarcoma cells

**Figure 1-source data 2:** Sequencing read counts and fold-change values for individual sgRNAs in library experiments in A673 Ewing sarcoma cells

**Figure 1-source data 3:** Relative GFP positive percentages in negative selection sgRNA assays in 6 independent pediatric sarcoma cell lines

**Figure 1-source data 4:** Relative GFP positive percentages in negative selection sgRNA assays in BRD9-FL, BRD9-Dbromo or BRD9-N216A rescue experiments performed in HSSYII cells

1263

1264 **Figure 2:**

1265 **Figure 2-source data 1:** Mass spectrometry data from endogenous SS18-SSX1  
1266 purifications in HSSYII cells

1267

1268 **Figure 2-source data 2:** Mass spectrometry data from endogenous SS18-SSX2  
1269 purifications in SYO1 cells

1270

1271 **Figure 2-source data 3:** Fold depletion of GFP positive cells in negative selections  
1272 sgRNA assays in HSSYII and SYO1 cells in BRD9 sgRNA tiling experiments

1273

1274 **Figure 2-source data 4:** Relative GFP positive percentages in negative selection  
1275 sgRNA assays in BRD9-FL, BRD9-D311-345 rescue experiments performed in  
1276 HSSYII cells

1277

1278 **Figure 4:**

1279 **Figure 4-source data 1:** ChIP-qPCR data of HA-tagged BRD9 proteins - BRD9-FL,  
1280 BRD9  $\Delta$ bromo and BRD9  $\Delta$ 311-345 - expressed in HSSYII cells.

1281 **Figure 5:**

1282 **Figure 5-source data 1:** Induction of apoptosis in HSSYII and SYO1 cells treated  
1283 with dBRD9-A at 100nM over 9-days.

1284

1285 **Figure 5-source data 2:** Cell cycle dynamics of HSSYII and SYO1 cells treated with  
1286 dBRD9-A at 100nM over 9-days.

1287

1288 **Figure 5-source data 3:** Gene expression changes in HSSYII cells treated with  
1289 dBRD9-A at 100nM for 6hrs

1290

1291 **Figure 2-figure supplement 1:**

1292 **Figure 2-figure supplement 1-source data 1:** Mass spectrometry data from SS18-  
1293 SSX1 purifications in HEK293T cells

1294

1295 **Figure 2-figure supplement 1-source data 2:** Mass spectrometry data from SS18-

1296 SSX2 purifications in HEK293T cells

1297

1298 **Figure 2-figure supplement 1-source data 3:** Presented is the number of peptides  
1299 mapping to each of the indicated BAF complex members in purifications of HA-  
1300 tagged SS18-SSX1 and SS18-SSX2 expressed in HEK293T cells

1301

1302 **Figure 2-figure supplement 1-source data 4:** Presented is the number of peptides  
1303 mapping to each of the indicated BAF complex members in purifications of  
1304 endogenous SS18-SSX1 and SS18-SSX2 expressed in HSSYII and SYO1 cells

1305

1306 **Figure 4-figure supplement 1:**

1307 **Figure 4-figure supplement 1-source data 1:** Fold-change of individual BAF  
1308 complex members identified in SS18-SSX1 purifications from HSSYII cells treated  
1309 with DMSO or dBRD9-A at 100nM for 24hrs

1310

1311 **Figure 5-figure supplement 1:**

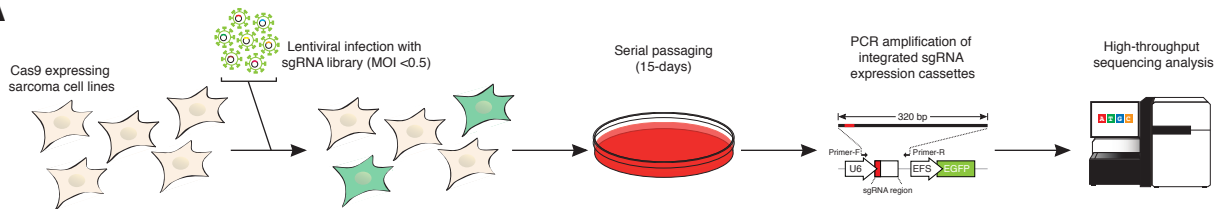
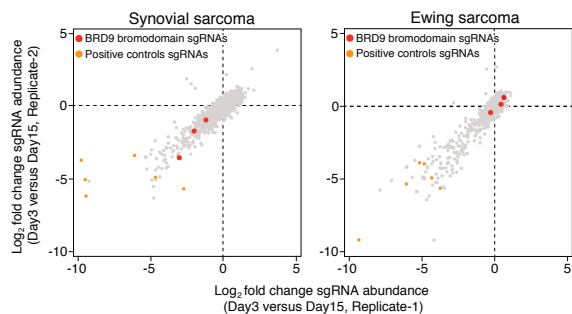
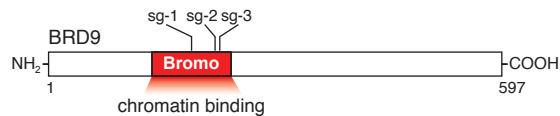
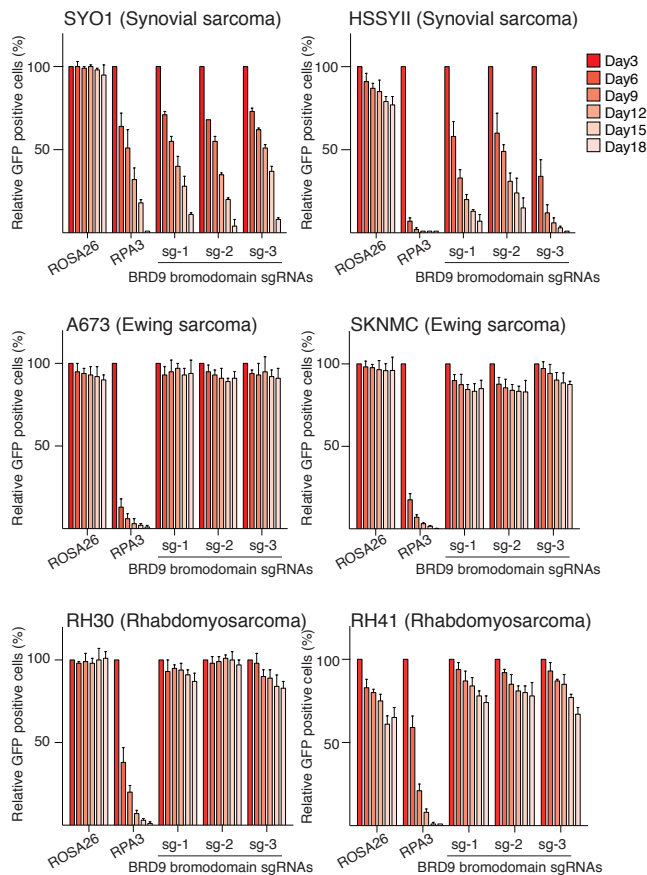
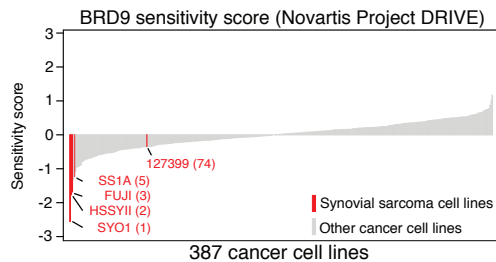
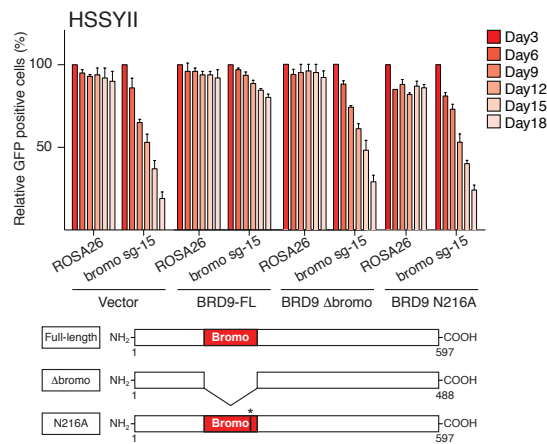
1312 **Figure 5-figure supplement 1-source data 1:** Cell counts in dBRD9-A treatment  
1313 experiments in HSSYII cells infected with an empty vector, a WT BRD9 expressing  
1314 vector or a BRD9 bromodomain swap (BRD7 bromodomain) vector

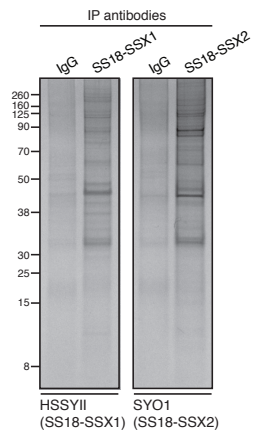
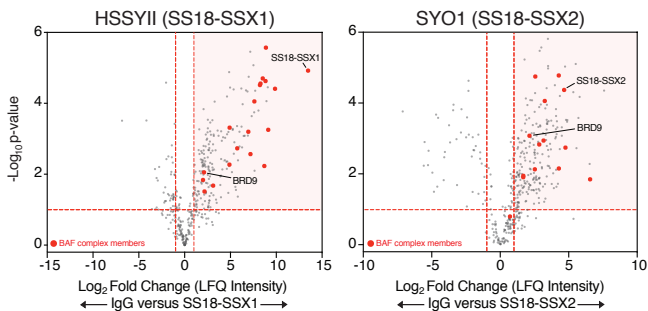
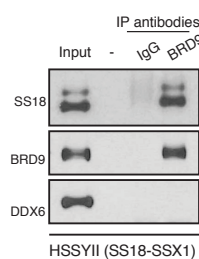
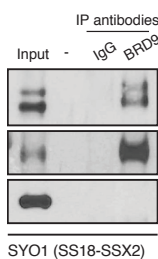
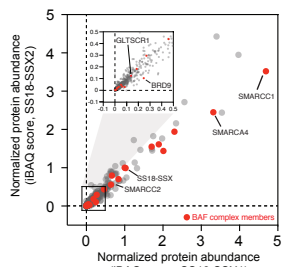
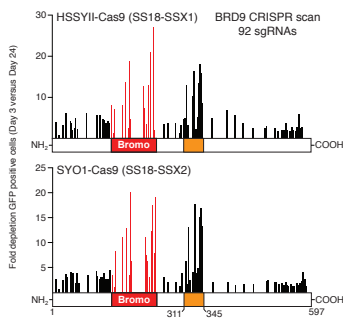
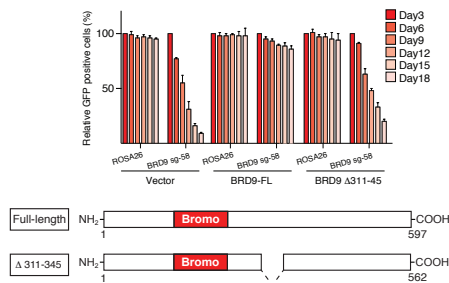
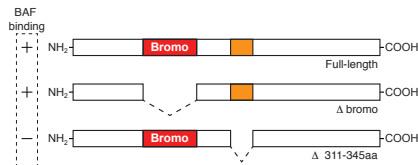
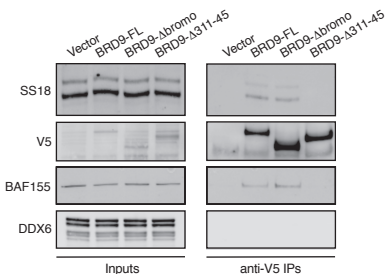
1315 **Figure 5-figure supplement 1-source data 2:** Mouse weight measurement derived  
1316 from mice treated with control (vehicle) of dBRD9-A at 50mg/kg

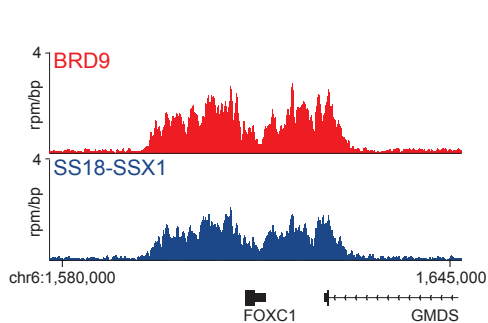
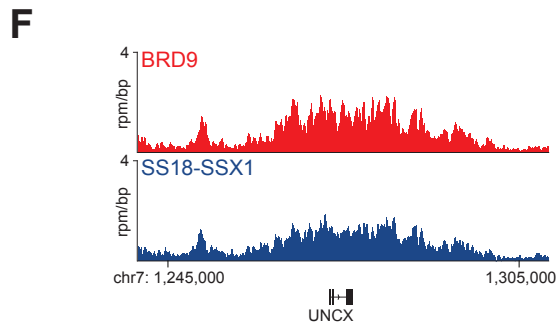
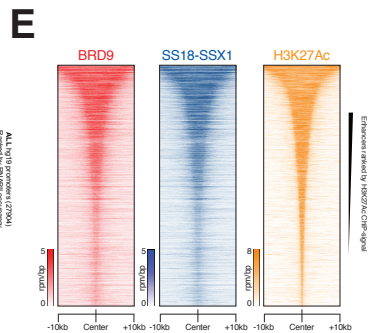
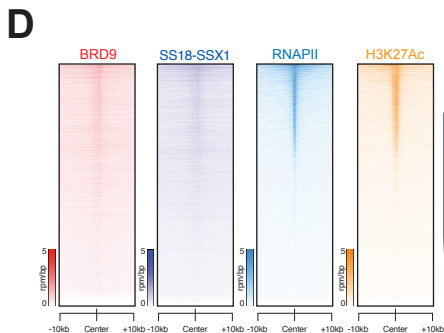
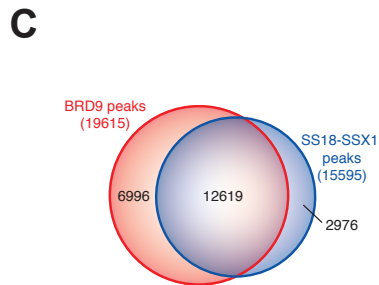
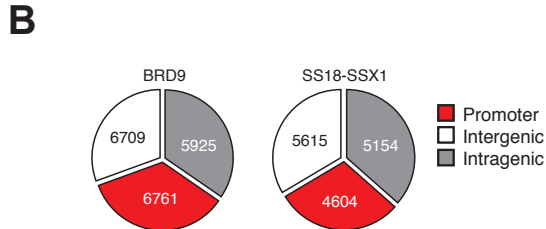
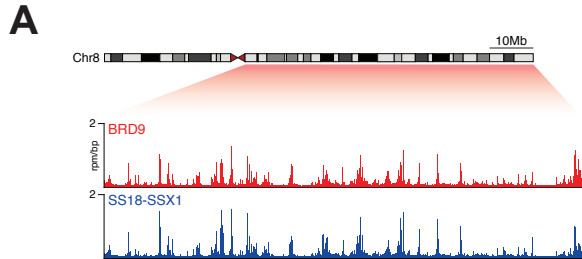
1317

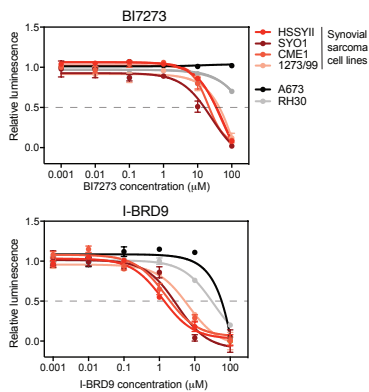
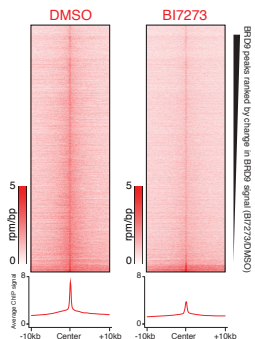
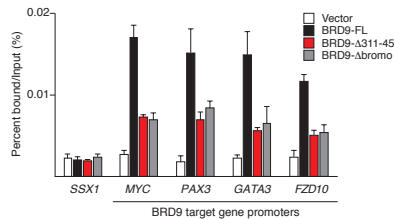
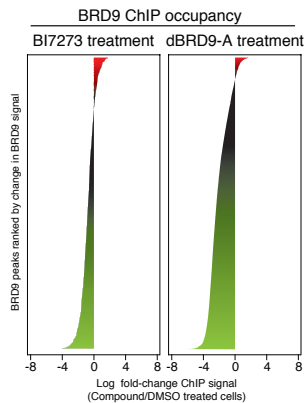
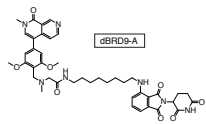
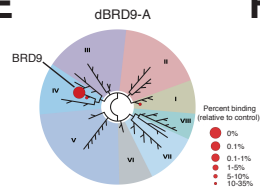
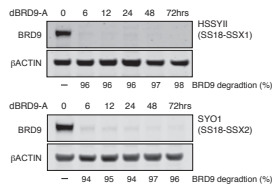
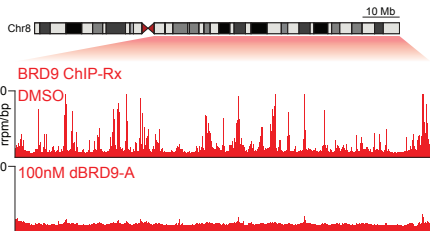
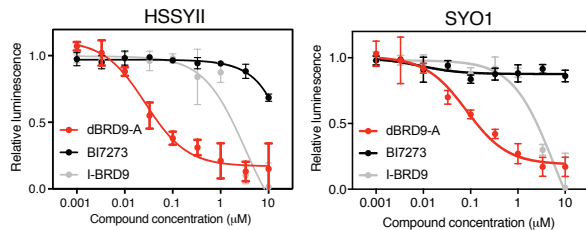
1318 **Figure 5-figure supplement 1-source data 3:** Presented are blood counts derived  
1319 from DMSO and dBRD9-A treated mice 1 day prior to cessation of treatment

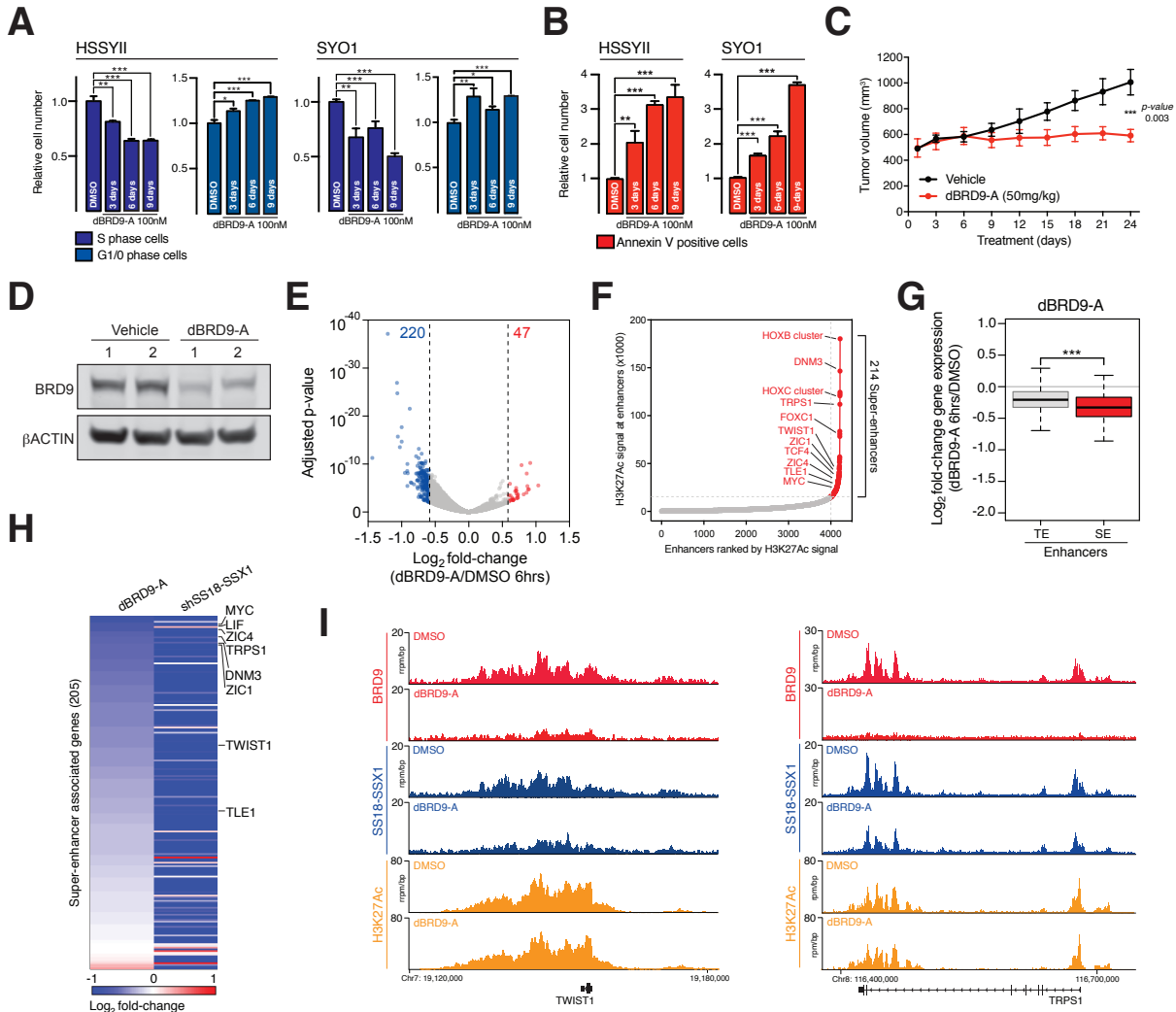


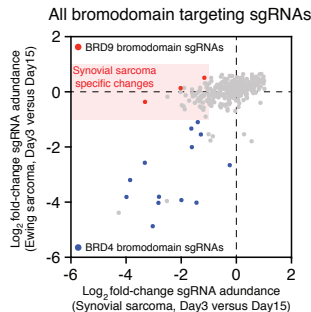
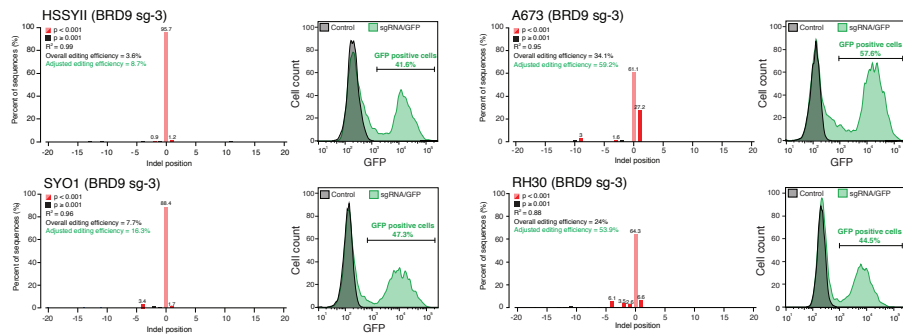
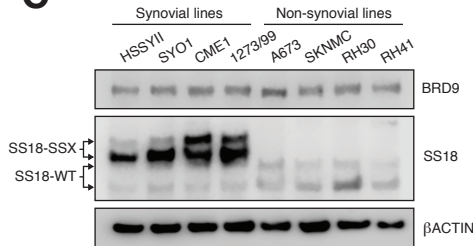
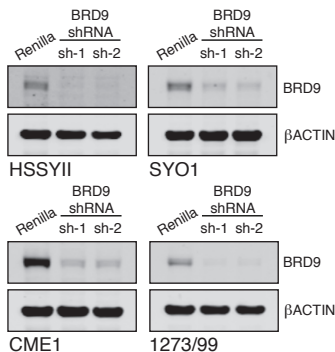
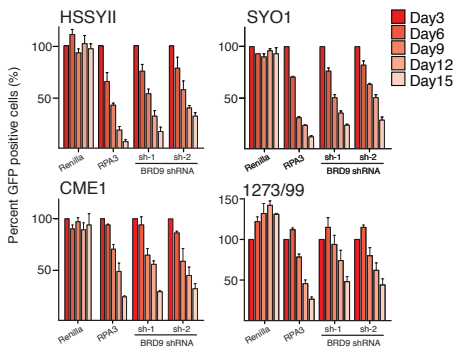
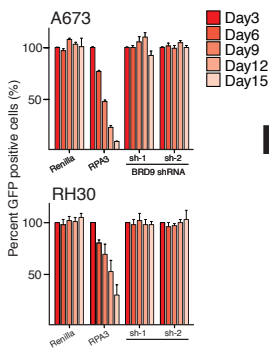
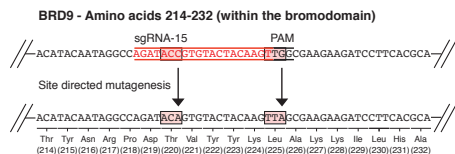
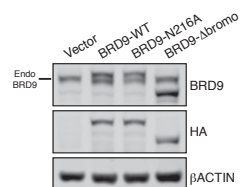
**A****B****C****D****E****F**

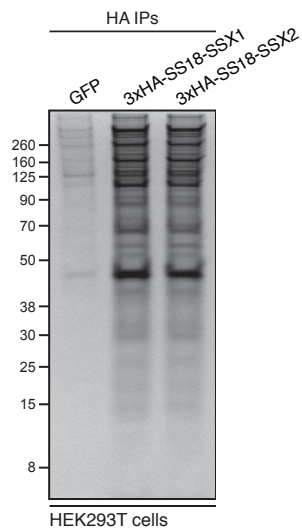
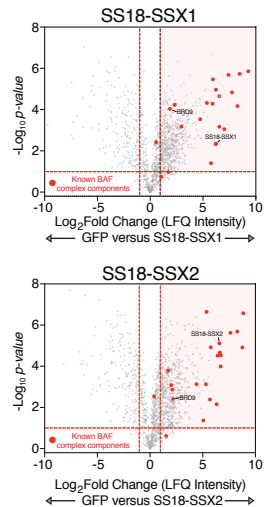
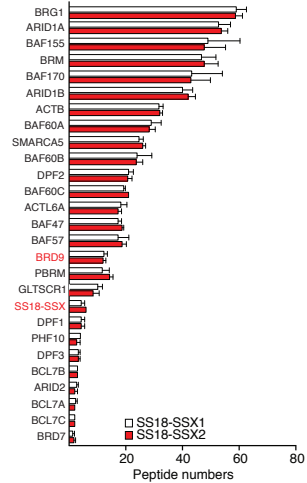
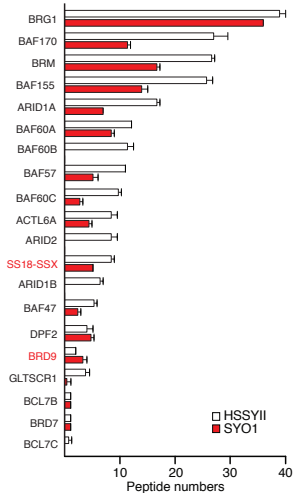
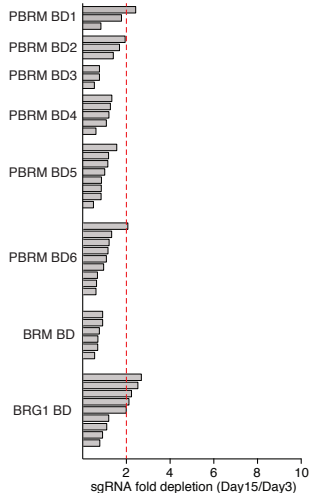
**A****B****C****D****E****F****G****H**

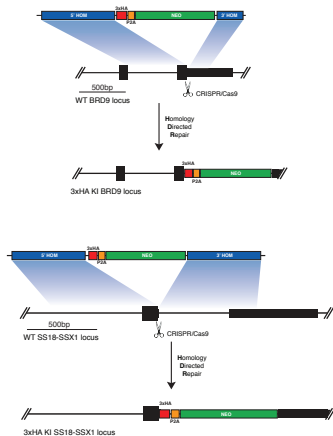
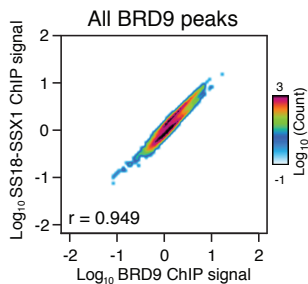


**A****B****C****G****D****E****F****H****I**

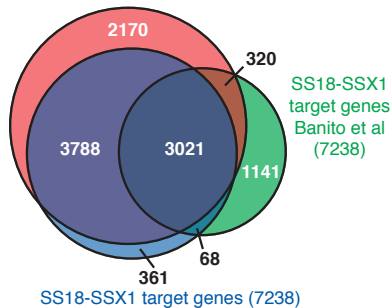


**A****B****C****D****E****F****G****H****I**

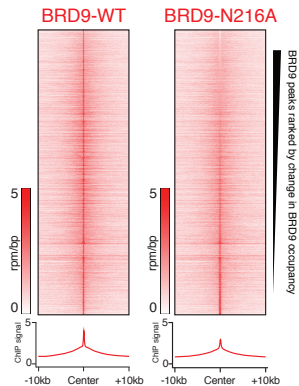
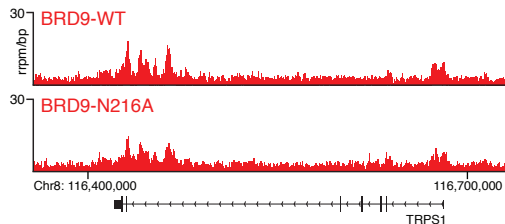
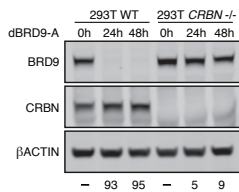
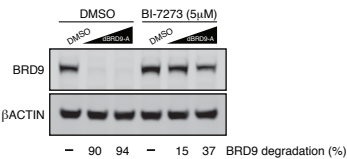
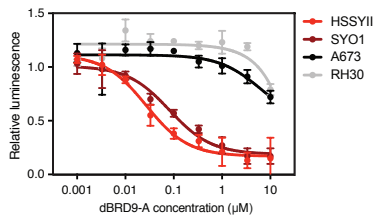
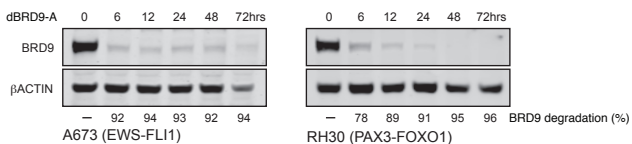
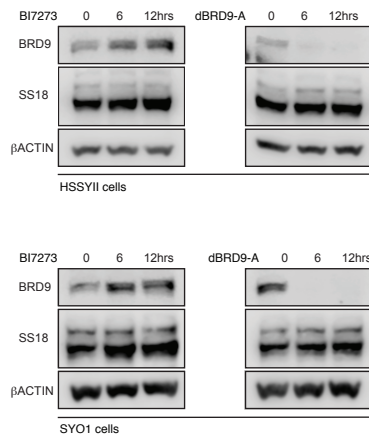
**A****B****C****D****E**

**A****B****C**

BRD9 target genes (9299)





**A****B****C****D****E****F****G****H**